Experimental Investigation on the Transport of Sulfide Driven by Melt-rock Reaction in Partially Molten Peridotite

Zhenjiang Wang[1,3], Zhuo-sen Yao[2], Zhenmin Jin[3], Yannan Wang[1]

[1]Key Laboratory of Resource Exploration Research of Hebei Province, and School of Earth Science and Engineering, Hebei University of Engineering, 056038 Handan, China.

[2]State Key Laboratory of Geological Processes and Mineral Resources, and School of Earth Resources, China University of Geosciences, 430074 Wuhan, China.

[3]State Key Laboratory of Geological Processes and Mineral Resources, and School of Earth Sciences, China University of Geosciences, 430074 Wuhan, China.

Corresponding author: Zhuo-sen Yao and Zhenmin Jin (yaozhuosen@cug.edu.cn; zmjin@cug.edu.cn)

Key Points:

- Systematical variations in lithologies and compositions of silicate minerals and melts during melt-peridotite reaction
- Flow behavior of melts around sulfide droplets through melt channel or pore throat in crystal framework of partially molten peridotite
- Upward extrusion and entrainment of sulfide droplets driven by focused melt flow with high velocity through narrow pore throats

Abstract

Extraction of sulfide liquid from partially molten mantle is vital to elucidate the cycling of metal and sulfur elements between different geochemical circles but has not been investigated systematically. Using the reaction couple method of laboratory experiments and theoretical calculations, this study documents systematical variations in lithologies and compositions of silicate minerals and melts, which are approximately consistent with the results of thermodynamically-constrained model. During melt-peridotite reaction, dissolution of olivine and precipitation of new orthopyroxene produce an orthopyroxene-rich layer between melt source and peridotite. With increasing reaction degree, more melt is infiltrated into and reacts with upper peridotite, which potentially enhances the concomitant upward transport of dense sulfide droplets. Theoretical analyses suggest an energetical focused melt flow with a high velocity (~ 170.9 μm/h) around sulfide droplet through pore throat. In this energic melt flow, we, for the first time, observed the mechanical coalescence of sulfide droplets, and produced drag force was likely driving upward entrainment of fine μm-scale sulfide. For coarse sulfide droplets whose sizes are larger than the pore throat in partially molten peridotite, their entrainment through narrow constrictions in crystal framework seems to be physically possible only when high-degree melt-peridotite reaction drives high porosity of peridotite and some channelized melt flows with extremely high velocity. Hence, melt-rock reaction could drive and enhance upward entrainment of μm- to mm-scale sulfide in the partially molten mantle, potentially contributing to the fertilization of the sub-continental lithospheric mantle and the endowment of metal-bearing sulfide for the formation of magmatic sulfide deposits.

Plain Language Summary

Sulfides are a pivotal potential reservoir for sulfur and economically important metals. Their transport in the Earth's mantle plays a vital role in understanding many crucial geological and environmental processes, especially the formation of mineral deposits, and the environmental damage and health hazards related to volcanic eruptions. This work proposes a new driving force for upward transport of dense sulfide drops in the upper mantle that experiences partial melting. Reaction between melt and rock potentially leads to focused melt flow in new-forming channels with three orders of magnitude higher velocity than that of melt flowing among crystal framework of peridotite. This energetic melt flow drives upward transport of tiny μm-scale

sulfide droplets in peridotite and may also facilitate amalgamation of droplets contacting each other. Coarse sulfide droplets could be possibly entrained upward through narrow pore throats, especially when high-degree melt-peridotite reaction drives fast-flowing melt in the mantle with high porosity.

1 Introduction

Sulfide is ubiquitous in mantle rocks (Alard et al., 2011) and an important repository for sulfur and geochemically and economically important chalcophile metals, which plays an important role in the partitioning behaviors of PGE, Cu, and Ni (Mungall & Brenan, 2014; Patten et al., 2013). Understanding the factors that control the fate of sulfide phases in the partially molten mantle is of fundamental importance in exploring the recycling of sulfur and chalcophile elements among different geochemical reservoirs (Ding & Dasgupta, 2017; Farquhar et al., 2002; Yao et al., 2018; Chen et al., 2022) and identifying the re-fertilization of the depleted lithospheric mantle, potentially providing the metal endowment for the formation of Cu-rich porphyry and/or Ni-rich magmatic ore system (Holwell et al., 2022; Lee & Tang, 2020; Mungall et al., 2015; Zhao et al., 2022). However, it remains highly contentious for driving forces of the transport of metal-bearing sulfide liquid, which severely blocks our understanding of the details of fertilization processes occurred in the source of sulfide-related magmatic and hydrothermal deposits.

Conventionally, the removal of sulfide liquid from a partially molten peridotite requires sulfide liquid to be progressively dissolved by the departing silicate melt (Holzheid & Grove, 2002; Mungall & Brenan, 2014; Yao et al., 2018). Nevertheless, the mechanical entrainment of sulfide liquid could also potentially be an efficient process driving the redistribution and local enrichment of sulfur and chalcophile elements in the mantle source (Iacono-Marziano et al., 2022; Heinrich & Connolly, 2022; Z. Wang et al., 2020; Yao & Mungall, 2020). Although a small amount (< percolation thresholds) of sulfide liquid under hydrostatic conditions cannot be entrained through the porous flow of silicate melt due to the high surface tension (Bagdassarov et al., 2009; Holzheid et al., 2000; Yoshino et al., 2003, 2004), it has been argued that the extraction of sulfide liquid driven by stress in a partially molten peridotite could be further facilitated by the directional porous flow of silicate melt, strongly affecting the fractionation and abundances of chalcophile metals in the mantle melting products, *i.e.*, basalts (Ballhaus et al.,

2006; Bockrath et al., 2004; Z. Wang et al., 2020). Except for the deviatoric stress, a preliminary experimental study (Wang & Jin, 2020) proposed that during melt-rock reaction, the entrainment of sulfide liquid may be enhanced by the reaction infiltration instability (RII) in the partially molten peridotite when a reacting melt percolates through a dissolvable, porous, melt-mineral mixture. The mechanical transport and enrichment of sulfide during this melt-rock reaction have been extensively demonstrated in mantle peridotites, which may clarify some geochemical paradoxes of the chalcophile/siderophile elements (Ciazela et al., 2018; Lorand & Luguet, 2016). The RII theory proposed by Chadam et al. (1986) also applies to magmatic systems by introducing viscous compaction of the matrix and driving a solubility gradient along the flow direction in place of the propagating reaction front (Aharonov, 1995), which induces positive feedback between the increasing permeability due to melt-rock reaction and the associated increase of melt flux in reacting regions. The reaction between peridotite and silicate melt is well known as a pervasive process even forming melt-rich channels with an extremely speedy melt flow due to the positive feedback in partially molten regions of the mantle, which has been broadly demonstrated by geological investigations (*e.g.*, Kelemen et al., 1995; Sundberg et al., 2010), high-temperature, high-pressure (HTHP) laboratory works (*e.g.*, Daines & Kohlstedt, 1994; Pec et al., 2015) and theoretical analyses (Aharonov, 1995; Chadam et al., 1986; Spiegelman et al., 2001). During a reaction of melt with a depleted mantle, melt re-fertilization processes potentially occur, thereby impregnating the mantle with sulfides, which have been widely found in mantle xenoliths, orogenic and abyssal peridotites (*e.g.*, Ciazela et al., 2018; Luguet et al., 2003; Niu, 2004; Wang et al., 2009).

Although it has been tentatively demonstrated that the rapid enough ascending magma flow in those melt-rich channels could hold upwards entrainment of large olivine phenocrysts or even dense sulfide droplets during the melt-rock reaction (Pec et al., 2017; Wang & Jin, 2020), the extraction of sulfide liquid driven by the RII has received very little attention, and the precise physical and chemical constraints during these processes appear to be worth studying thoroughly, which is vital to the fertilization of lithospheric mantle, as well as the formations of magmatic and/or hydrothermal sulfide deposits. Here we conducted systematically two-layer reaction experimental studies in which a partially molten peridotite is placed on a sulfide-bearing silicate melt source to explore the entrainment of sulfide liquids driven by the RII and the physical and chemical changes of liquid and solid phases during these processes.

2 Materials and Methods

2.1 Starting materials

As a melt source, the starting materials were a mixture of the powdered calc-alkaline tholeiitic basalt (70 wt.%) from the East Pacific Rise (102.7044 °W, 2.64961 °S), olivine crystals (20 wt.%) from fresh spinel lherzolite xenoliths at Damaping (Hannuoba region), North China, and sulfide aggregates (10 wt.%) from Jinchuan Ni-Cu sulfide deposit, NW China. Additionally, 0 or 2 wt.% oceanic sediments (mainly carbonate) were mixed into the melt source to explore the effect of volatile (CO_2) on the transport of sulfides. The Ni-Cu sulfides were composed of pyrrhotite (59 wt.%), pentlandite (36 wt.%), and chalcopyrite (5 wt.%) separates, similar to the composition of base-metal sulfide aggregates in massif peridotites (Lorand et al., 2010), and were grounded in alcohol for about 6h to < 10 μm measured by using the scanning electron microscope (SEM).

To prepare a partially molten rock, olivine and clinopyroxene crystals from Damaping spinel lherzolite xenoliths were mixed in a 50:50 ratio by weight. Subsequently, ~ 0 or ~ 5 wt.% calc-alkaline tholeiitic basalts were added to change the initial permeability of the partially molten rock. All silicate mineral grains were ground to 10-20 μm grain size in an agate mortar.

The partially molten rock was placed on the melt source, and the length ratio of these two parts was slightly larger than ~1:1 to avoid chemical equilibration between the melt source and the partially molten rock over experimental time scales. Compositions of these starting materials were described by Z. Wang et al. (2020), and experimental conditions are listed in Table 1.

Table 1. Summary of experimental conditions and observed lithologies.

NO.	Starting material (upper peridotite/lower melt source)	Experimental conditions (P/GPa, T/°C, t/h)	Capsule	Lithologies (upper peridotite/reaction interface /melt source)
PC520	Ol:Cpx(1:1)/Ol(20%)+basalt(70 %)+sulfide(10%)	1.5,1250,12	Pt-graphite	Ol+Cpx+SM+SL/ORL (Opx+SM+SL)/ Opx+SM+SL
PC527	Ol:Cpx(1:1)/Ol(20%)+basalt(70 %)+sulfide(10%)	1.5,1300,12		Ol+Cpx+SM+SL/olivine-melt layer (Ol+SM+SL)/ORL (Opx+SM+SL)/ Opx+SM+SL
PC528	Ol:Cpx(1:1)/Ol(20%)+basalt(70 %)+sulfide(10%)	1.5,1250,48		Ol+Cpx+SM+SL/ORL (Opx+SM+SL)/ Opx+SM+SL
PC537	Ol:Cpx(1:1)/Ol(20%)+basalt(70 %)+sulfide(10%)	1.5,800,12		Ol+Cpx/Ol+basalt+sulfide

PC545	Ol:Cpx(1:1)/Ol(20%)+basalt(70%)+sulfide(10%)	1.5,1250,72		Ol+Cpx+SM+SL/olivine-melt layer (Ol+SM+SL)/ORL (Opx+SM+SL)/Opx+SM+SL
PC548	Ol:Cpx(1:1)+basalt(5wt%)/Ol(20%)+basalt(70%)+sulfide(10%)	1.5,1250,48		Ol+Cpx+SM+SL/ORL (Opx+SM+SL)/Opx+SM+SL
PC559	Ol:Cpx(1:1)+basalt(5wt%)/Ol(20%)+basalt(70%)+sulfide(10%)	0.5,1200,6		Ol+Cpx+SM+SL/Ol+SM+SL
PC560	Ol:Cpx(1:1)+basalt(5wt%)/Ol(20%)+basalt(68%)+carbonate(2%)+sulfide(10%)	1.5,1250,24		Ol+Cpx+SM+SL/olivine-melt layer (Ol+SM+SL)/ORL (Opx+SM+SL)/Opx+SM+SL

Note: Ol-olivine; Cpx-clinopyroxene; SM-silicate melt; SL-sulfide liquid; ORL-orthopyroxene-rich reaction layer

2.2 Experimental methods

The two-layer reaction experiments were conducted at the State Key Laboratory of Geological Processes and Mineral Resources (GPMR) of China University of Geosciences using a 150 Ton non-end-loaded type piston-cylinder press. Starting materials were loaded into a 3.75-mm-diameter and 5-6-mm-high cylindrical platinum (Pt) capsule with a graphite inner sleeve (Figure 1-inset in the lower left). In this assembly, the sample was in contact only with the graphite inner sleeve and therefore, the oxygen fugacity of this experimental system was maintained at about CCO-0.8 (the graphite-CO_2 buffer), which corresponds to a log fO_2 < FMQ-2 log unit at ~1360 °C and 1.5 GPa (*e.g.*, Médard et al., 2008). A low friction assembly consisting of NaCl and Pyrex sleeves, a graphite heater, sintered MgO spacers, and an Al_2O_3 plug, was used for the piston-cylinder experiments. Pressure calibration was conducted against the quartz/coesite phase transition, and was accurate to ± 0.1 GPa. The temperature was monitored by a W/Re type C thermocouple located at the bottom of the capsule. These experiments (Table 1) were conducted under pressures of 0.5-1.5 GPa and temperatures of 800-1300 °C for 12-72 h before being quenched to room temperature. All capsules were heated before being sealed at 120 °C in a vacuum oven for more than 12 h to remove absorbed water vapor in the specimens, and no apparent sulfur loss was observed during this drying.

2.3 Analytical techniques

Polished sections were prepared from the recovered experimental specimens cut parallel to the specimen axis. The microstructure of experimental run products was observed using a Quanta 450 field-emission scanning electron microscope (FE-SEM) at the GPMR with an

accelerating voltage of 20 kV, a spot size of 6.0 μm, and a working distance of ~ 12 mm. The backscattered electron (BSE) images were used to measure the morphological characteristics of experimental products, such as the thickness of reactive boundary layers, the dissolution distance, and the size of sulfide droplets.

Quantitative compositional analyses for olivine and clinopyroxene were performed using a JEOL JXA-8230 electron probe microanalyzer with four wavelength-dispersive spectrometers (WDS) at the Center for Global Tectonics, School of Earth Sciences, China University of Geosciences (Wuhan). Fifteen kV accelerating voltage, 20 nA probe current, and a 1 μm beam diameter had been used. Sulfides were analyzed with 20 kV acceleration voltage and 20 nA beam current, whereas quenched silicate melts were analyzed with 15 kV/10 nA. A defocused beam of 20-30 μm diameter was used for all the standardizations and quenched melts and sulfides.

3 Results

Several two-layer reaction experiments (Table 1) were conducted at 0.5-1.5 GPa, 800-1300 ℃, and 12-72h to investigate the transport of sulfide liquid during reaction infiltration of silicate melt. Generally, several distinct lithological regions were developed and, from bottom to top, respectively separated by a diffuse-dominated, mineralogical interface in these two-layer reaction experiments (Figure 1). All two-dimensional images were analyzed using the freeware ImageJ developed by the National Institute of Health (NIH) (http://imagej.nih.gov/ij/).

3.1 Phase assemblages and textures

Under the low-temperature, high-pressure conditions (800 ℃ and 1.5 GPa), both minerals and sulfides were generally polygonal and not molten, and sulfide droplets in the lower part of the sample were uniformly distributed in pores among silicate grains. At 1.5 GPa, when the experimental temperatures exceed ~1250 ℃, the basaltic material was completely molten, and the diameter of sulfide droplets ranges from several μm to > 100 μm (Figure 1). Gravitational segregation of sulfide was hardly ever observed in all samples, but obviously, some huge sulfide droplets were attached to the graphite capsule wall, especially at high-temperature conditions (Figure 1). These coarse droplets were removed from the collected data to estimate the average droplet size. Tiny exsolution lamellae with higher backscattered electron (BSE)

intensity were occasionally observed in some quenched large sulfide droplets. Sometimes silicate melts were pooled at the edge of sample (Figure 1).

In all high-pressure experiments (1.5 GPa), orthopyroxene (Opx)-rich reaction layer (ORL) was formed between the lower melt source and the upper partially molten peridotite due to the reaction between them, and it chiefly consists of Opx grains, silicate melt, and sulfide droplets (Figure 1). With increasing the annealing time and/or run temperature, the morphology of ORLs became more irregular (Figure 2), and the ORL at 1300℃ was even ruptured due to the presence of several enormous Opx grains (> 100 μm) with few or no sulfide inclusions (Figure 2b). We also observed the bulge of ORL toward the melt source (Figure 1), which can be attributed to the volumetric shrinkage of the melt source after being molten and the upward percolation of silicate melt. Thus, the original interface between the melt source and peridotite before the experimental reaction cannot be marked by the offset of the graphite inner sleeve. At 1250 ℃, the thickness of ORL increases from ~ 118.4 ± 11.1 μm (1σ) at 12h to ~ 416.3 ± 118.6 μm at 72h, which is likely a linear function of the square root of the run duration (slope = 0.78 ± 0.05) (Figure 3a-blue line). At 1300 ℃, the thickness increases considerably to 500.3 ± 127.9 μm at 12h (Figure 3a). Additionally, based on the linear fit, the addition of 5 wt.% basalts into the partially molten peridotite (run PC548) and/or 2 wt.% oceanic sedimentary into the melt source (run PC560) seems to have no significant effect on the thickness of ORL (Figure 3a).

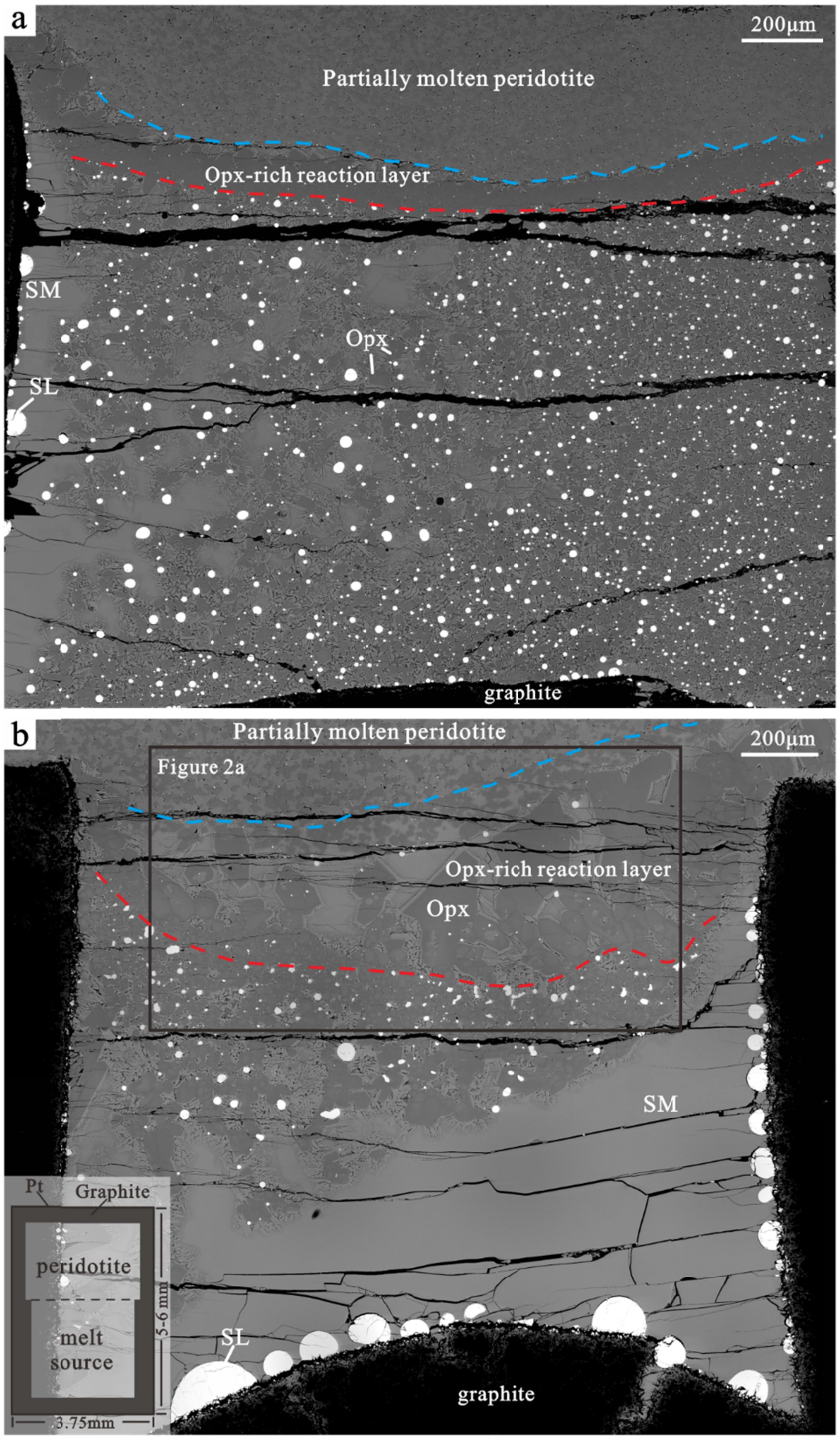

202

203 **Figure 1**. Back-scattered electron images (BSE) of experimental products from experiment
204 PC520 (a) (annealing time ~ 12h) and PC545 (b) (annealing time ~ 72h) under the conditions of
205 1.5 GPa and 1250 ℃. Red and blue dotted lines respectively denote the original and current
206 interfaces between the melt source and peridotite before and after the melt-rock reaction,

marking the Opx-rich reaction layer due to the melt-rock reaction. The region between the melt source and partially molten peridotite of experiment PC545 is exaggerated to observe the microstructure of the melt-rock reaction interface in Figure 2a. The specimen setup of these experiments is shown as the inset in the left lower part. Mineral abbreviations: Opx-orthopyroxene; SM- silicate melt; SL-sulfide liquid.

On the other hand, peridotites in the upper part of sample were in disequilibrium with silicate melt at these run conditions, thereby should be dissolved essentially into the melt. The amount of dissolution can be indirectly quantified by the dissolution distance (Figure 3b), which is the distance between the current interface (Figure 1-blue dotted lines) and the original interface (Figure 1-red dotted lines) that is represented by a sharp decrease in the size of sulfide droplets. All these measurements were conducted around the central part of each experimental charge at least 5 times. Similarly, dissolution distance increases linearly with the square root of time (Figure 3b-blue line) at 1250 ℃, and the increase of temperature to 1300 ℃ significantly enlarges the dissolution distance (Figure 3b). The addition of oceanic sedimentary (PC560) and/or basalt (PC548) has no substantial effect on the dissolution distance (Figure 3b).

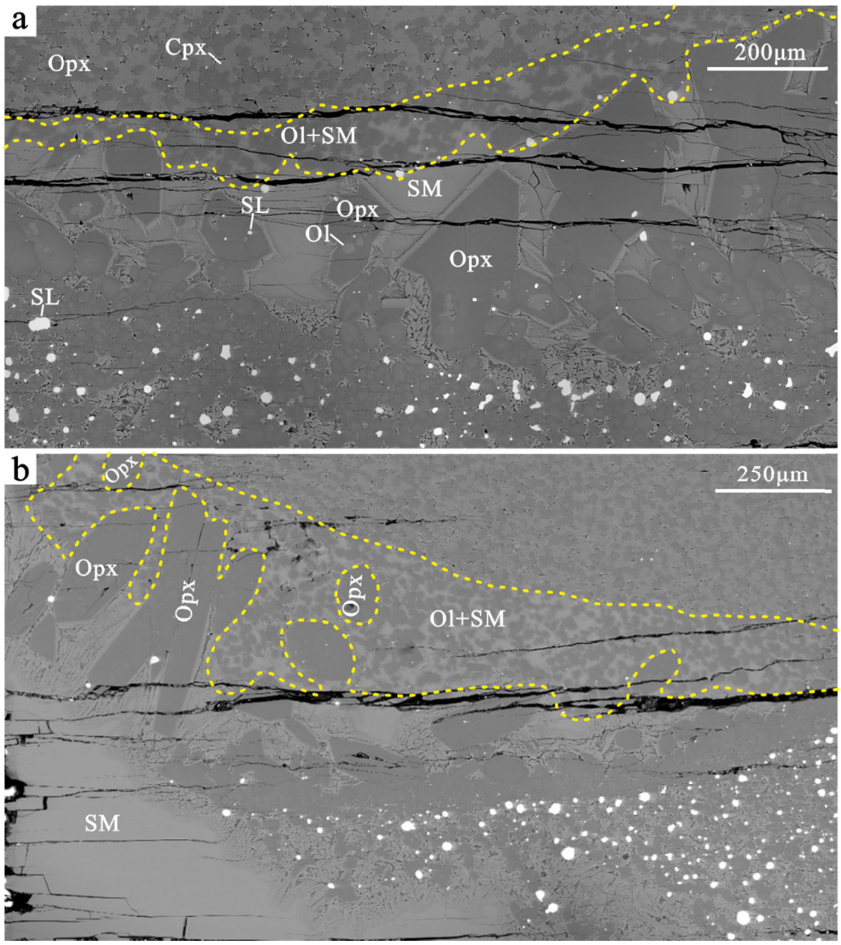
a
Opx
Cpx
200μm
Ol+SM
SM
SL
Opx
Ol
Opx
SL
b
Opx
250μm
Opx
Opx
Opx
Ol+SM
SM

222

Figure 2. Microstructures of the interface of melt-rock reaction in experiment PC545 (1250 ℃) (a) and PC527 (1300 ℃) (b). Yellow dotted lines show the olivine-melt layer consisting of olivine, sulfide, and silicate melt above the Opx-rich reaction layer. Mineral abbreviations: Ol-olivine. Note that some huge Opx grains are present in the Opx-rich reaction layer of experiment PC527 with high reaction temperature, leading to the destruction of the layer.

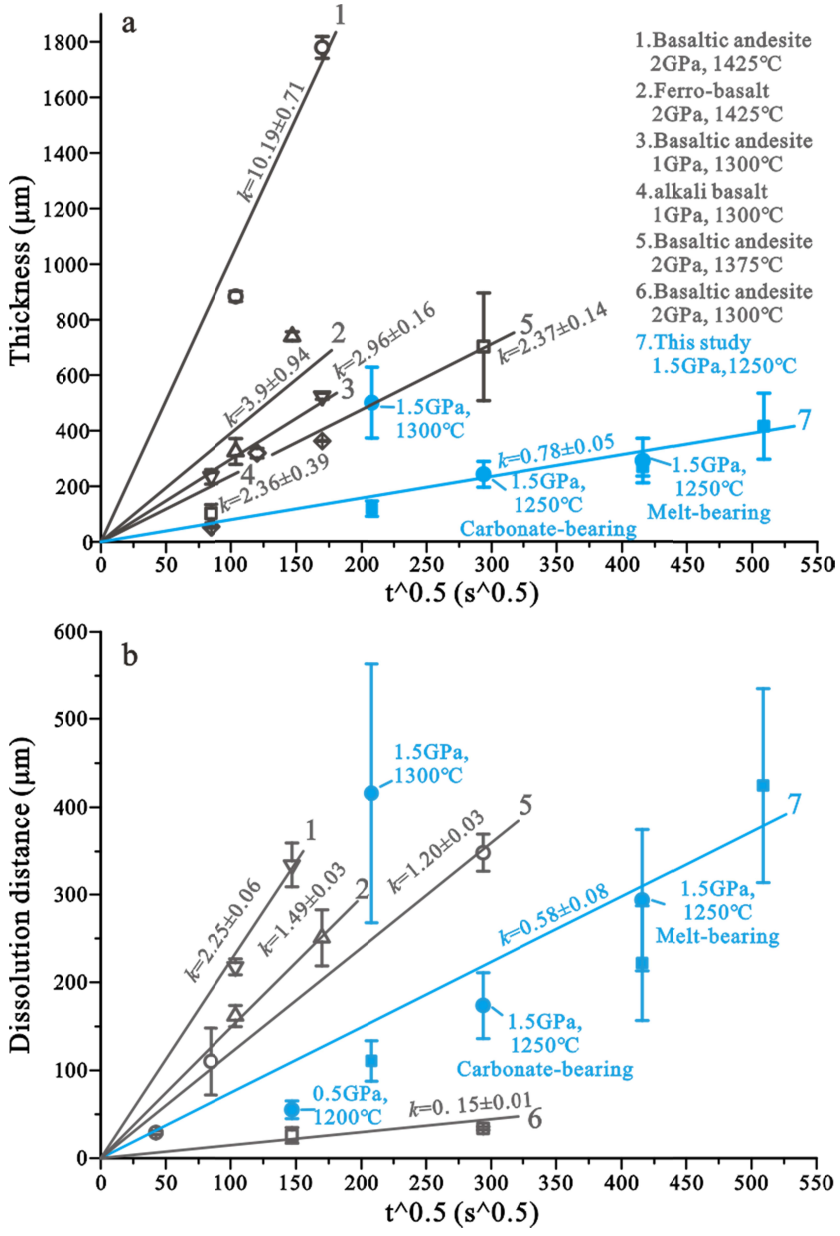

Figure 3. Plots of thicknesses of Opx-rich reaction layers (a) and dissolution distance (b) as a function of the square root of run time for the melt-rock reaction experiments. The lines are the

best fit for the data. The data denoted as 3 and 4 are from Morgan & Liang (2005), and other data are from C. Wang et al. (2020).

Moreover, based on analyses of SEM images, with increasing run duration or temperature, more silicate melt penetrated the Opx reaction layer into the partially molten peridotite (~ 4.65 ± 0.78 area% at 12h; ~ 7.13 ± 0.58 area% at 72h), resulting in the formations of melt junctions and channels among silicate minerals, and even some large melt pools just above the ORL (Figure 2 and Figure 4a). At 1.5 GPa, with increasing annealing time from 12h to 72h, the grain size of silicate minerals increases from 8.1 ± 3.4 μm to 11.0 ± 4.9 μm in the partially molten peridotite (Figure 4b; Supporting information; Table S1). Under conditions of high temperature (1300 ℃) and long-run duration (72h), an olivine-melt layer, consisting of sulfide, olivine, and silicate melt, is present above the ORL (Figure 2), which may be attributed to the dissolution of clinopyroxene and reprecipitation of olivine during the melt-peridotite reaction. Additionally, crystal faces between olivine grains were open and full of silicate melt, forming abundant melt channels among the crystal framework (Figure 2).

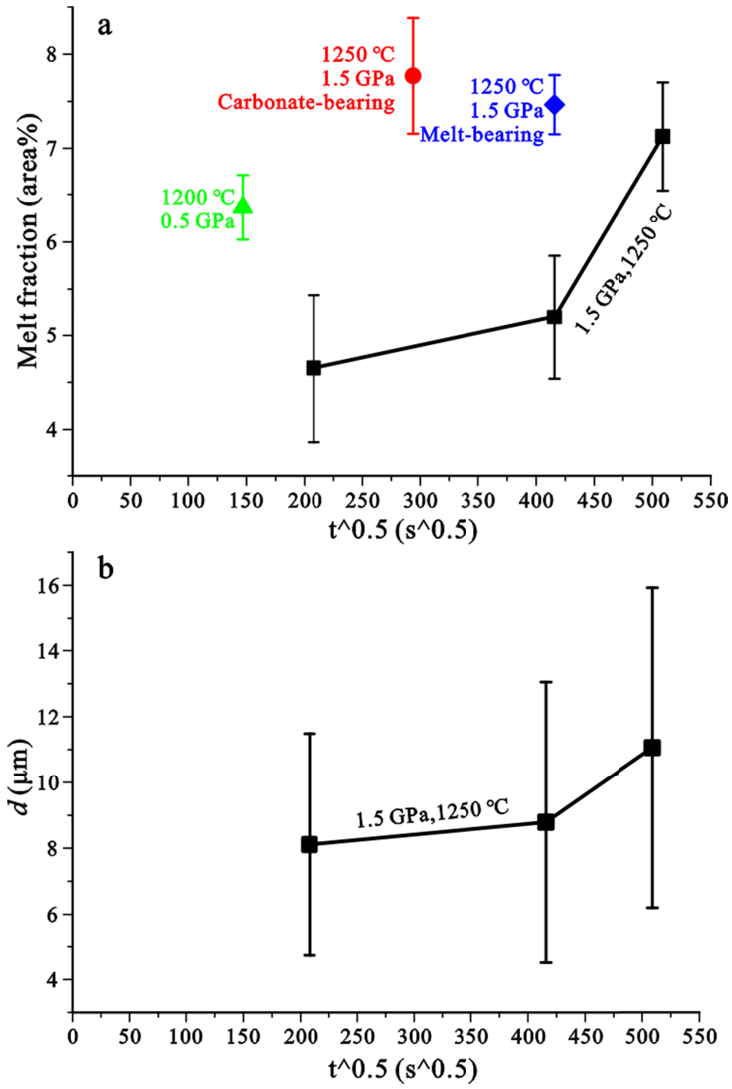

Figure 4. Plots of melt fraction (a) and grain size of silicate minerals (b) as a function of the square root of run time in the partially molten peridotite from these experiments of this study. Curves are drawn only to guide the eye.

In the melt source, the mean area-weighted diameter of sulfide droplets was ~ 4.1 ± 0.1 μm in a low-temperature hot-press experiment (PC537, 800 ℃), which potentially denotes the initial size of sulfide droplets in the starting material. At a higher temperature (1250 ℃), the sulfide size increases from ~ 14.7 ± 0.2 μm to ~ 49.4 ± 1.6 μm with increasing the annealing time from 12h to 72h (Figure 5a; Table S2), in which the larger standard deviations from the long annealing time (72h) experiments may be partly because of the presence of some enormous (> 50 μm) and tiny (< 1 μm) sulfide droplets. Under the same annealing time (48h), there is no

conspicuous increase in sulfide size when 5 wt.% basalt was added to the peridotite (PC548), while a slight increase was observed if the experimental temperature increased to 1300 ℃ (PC527) (Figure 5a). The addition of carbonate into the melt source (PC560) resulted in a significant increase in sulfide size to ~ 54.0 ± 1.6 μm at 24h (Figure 5a). Additionally, we also observed that the number density of sulfide droplets uniformly decreases with increasing annealing time in the lower melt source (Figure 5a-inset). The area fraction of sulfide liquid in the low-temperature experiment (800 ℃) was ~ 3.26 ± 0.12 area% of the melt source. At 1250℃, the area fraction was essentially constant (3.44 ± 0.14 area% at 12h; 3.50 ± 0.15 area% at 48h) when the annealing time was less than 48h, but a visible increase (5.46 ± 0.22 area%) can be observed for the experiments with annealing time of 72h (Figure 5b). A similar trend was also shown in the upper part of samples (Figure 5d), which may be due to more silicate melts from the melt source infiltrating into the upper part of samples with increasing annealing time to 72h (Figure 4). As previously observed (Yoshino & Watson, 2005), the diffuse addition of Fe and Ni components from silicate phases into sulfide liquids may be one of the reasons for the increase of the sulfide area fraction in the melt source. In contrast, with increasing temperature to 1300 ℃, a lower area fraction (2.93 ± 0.07 area %) of sulfide was observed even in the experiment with a short annealing time (12h) (Figure 5b), potentially due to partial dissolution of sulfide droplet driven by the higher sulfur content at sulfide saturation (SCSS) at a higher temperature (*e.g.*, Liu et al., 2007; Mavrogenes & O'Neill, 1999). Similarly, the additions of basalt and carbonate enhance the permeation of more silicate melt into the upper part of samples, thereby increasing the area fraction of sulfide in the melt source (Figure 5b).

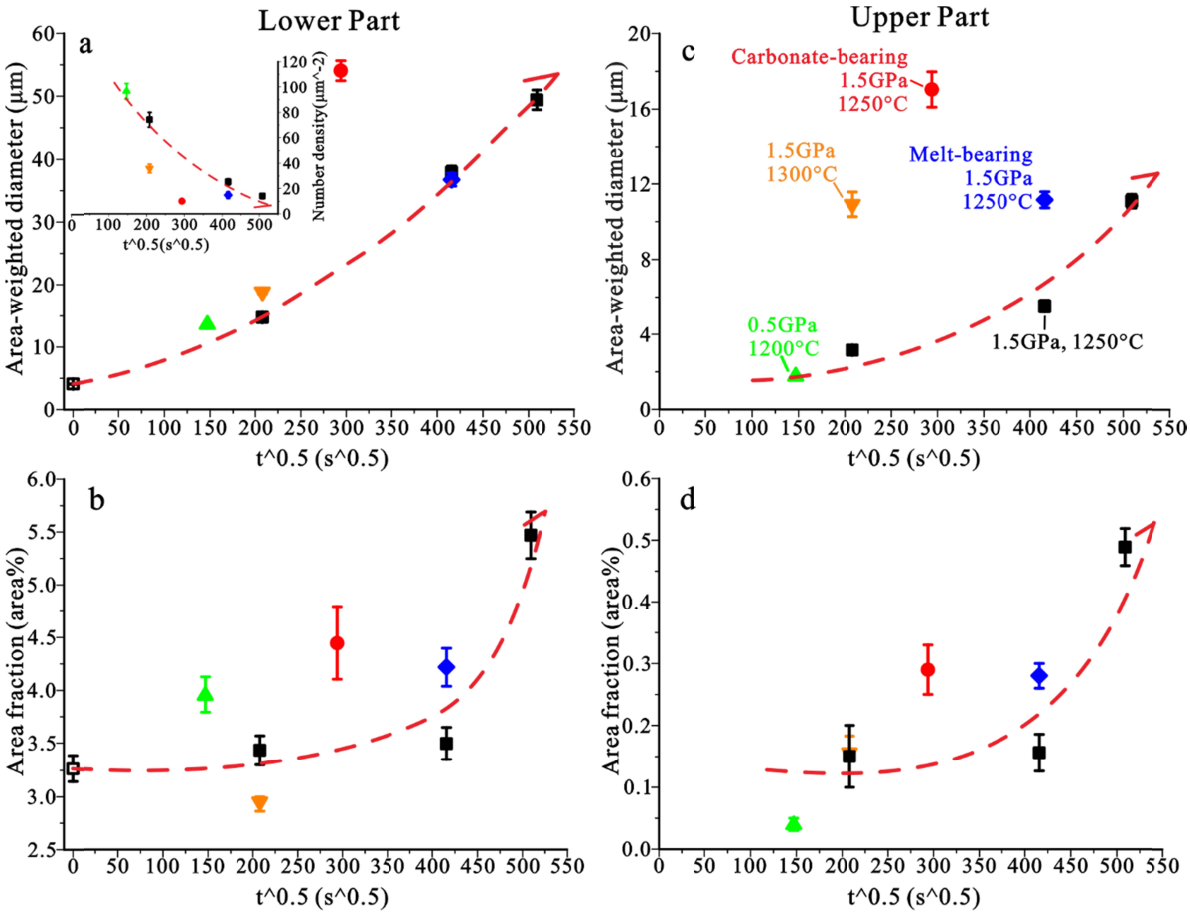

277

278 **Figure 5**. Plots of grain size (μm) of sulfide droplets weighted by the area (a and c) and area
279 fraction of sulfide droplets (b and d) as a function of the square root of run time in the melt
280 source (lower part) and the partially molten peridotite (upper part) from these experiments of this
281 study. Inset in (a) shows the relationship between the number density of sulfide droplets in the
282 melt source and the square root of run time. Curves are drawn only to guide the eye.

283 Based on the SEM images of products from these high-temperature experiments (1250
284 °C), it becomes evident that sulfide droplets in the melt source were entrained into the partially
285 molten peridotite by the porous flow of silicate melt during the melt-peridotite reaction (Figure
286 1b and Figure 2). With permeating more silicate melt upwards, more and larger sulfide droplets
287 were observed in the partially molten peridotite, and meanwhile their sizes (area-weighted
288 diameter ~ 3.1 ± 0.1 μm at 12h to ~ 11.1 ± 0.4 μm at 72h) and area fractions (~ 0.15 ± 0.05
289 area% at 12h to ~ 0.49 ± 0.03 area% at 72h) increase with the increasing annealing time at 1250
290 °C (Figure 5c and d; Table S2). Apparently, the addition of carbonate and 5 wt.% basalt into the
291 melt source and partially molten peridotite, respectively, drives a higher area fraction and larger

size of sulfide droplet in the upper part of samples (Figure 5c and d). Hence, these observations propose that the ORL may not efficiently prevents the upward transport of silicate melt and sulfide droplets from the melt source to the upper molten peridotite.

Notably, under the condition of lower pressure (0.5 GPa), some vapor bubbles have been found in the partially molten peridotite due to the exsolution of volatile (mainly H_2O) in the starting basaltic material, and they mostly absorb on sulfide droplets to form compound drops, which has been proposed to potentially enhance the upward transport of sulfide (Mungall et al., 2015; Yao & Mungall, 2020).

3.2 Phase compositions

3.2.1 Mineral compositions

Figure 6 and Figure 7 respectively showed the compositional variations of olivine and clinopyroxene as a function of distance away from the final melt-peridotite interface. Under conditions of 1.5 GPa and 1250-1300 ℃, from the far-field region to the interface, olivine grains became gradually lower in the Mg# (defined as molar Mg/(Mg+Fe)*100) and concentrations of SiO_2, MgO and NiO, and meanwhile had increased in FeO and MnO contents (Figure 6). Compared with the low-temperature hot-press experiment (PC537) (Figure 6 purple dotted lines), olivine grains from high-temperature experiments contained lower MgO and NiO, and higher FeO and CaO concentrations. By contrast, olivine compositions in the experiment PC548 (5 wt.% basalts) and PC559 (0.5 GPa) were roughly constant across the partially molten peridotite, whereas olivine grains crystallized in the melt source at lower-pressure (0.5 GPa, PC559) experiment had lower Mg#, MgO, SiO_2 and higher FeO than those in the peridotite region (Figure 6).

In contrast to olivine, more scatter compositions were observed in the clinopyroxene (Cpx) grains from the partially molten peridotite (Figure 7). Only near the melt-rock interface, the trends of decreasing Mg# and CaO and increasing FeO were present in Cpx from all high-pressure experiments, whereas the Cpx compositions in the low-pressure and carbonate-bearing experiment (PC559 and PC560) were essentially constant across the peridotite region (Figure 7). On the other hand, the Opx grains in the reaction layer and melt source were the products of

320 silicate melt-olivine reaction. No distinct compositional difference was observed in these Opx
321 grains.

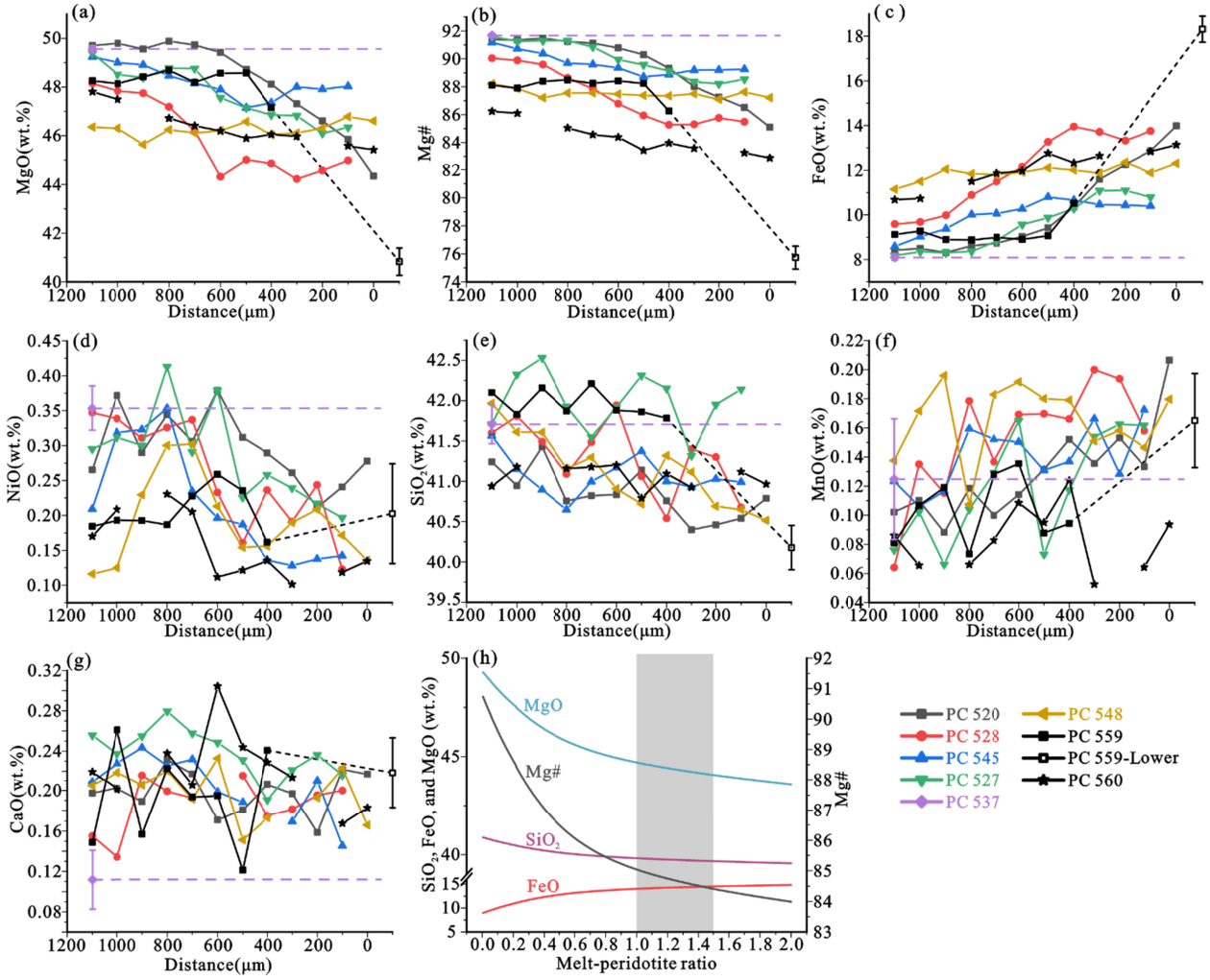

322

Figure 6. Plots (a-g) of measured oxide abundance (in wt.%) and Mg# in olivine as a function of distance (in μm) away from the melt-rock interface. The composition variations of MgO, Mg#, FeO, and SiO_2 are also simulated thermodynamically as a function of melt-peridotite ratio in (h). When the melt-rock ratio is between 1 and 1.5, these measured compositions are roughly consistent with those results simulated thermodynamically (the gray shadow region in h). At low pressure (PC559, 0.5 GPa), the compositions of olivine recrystallized in the melt source during the melt-rock reaction are present as PC559-Lower (black hollow square). The composition of olivine grains in the low-temperature hot-press experiment (PC537) was almost constant across the partially molten peridotite region and thus can be used as the reference line (purple dotted lines) for the composition variations of olivine in those high-temperature reaction experiments.

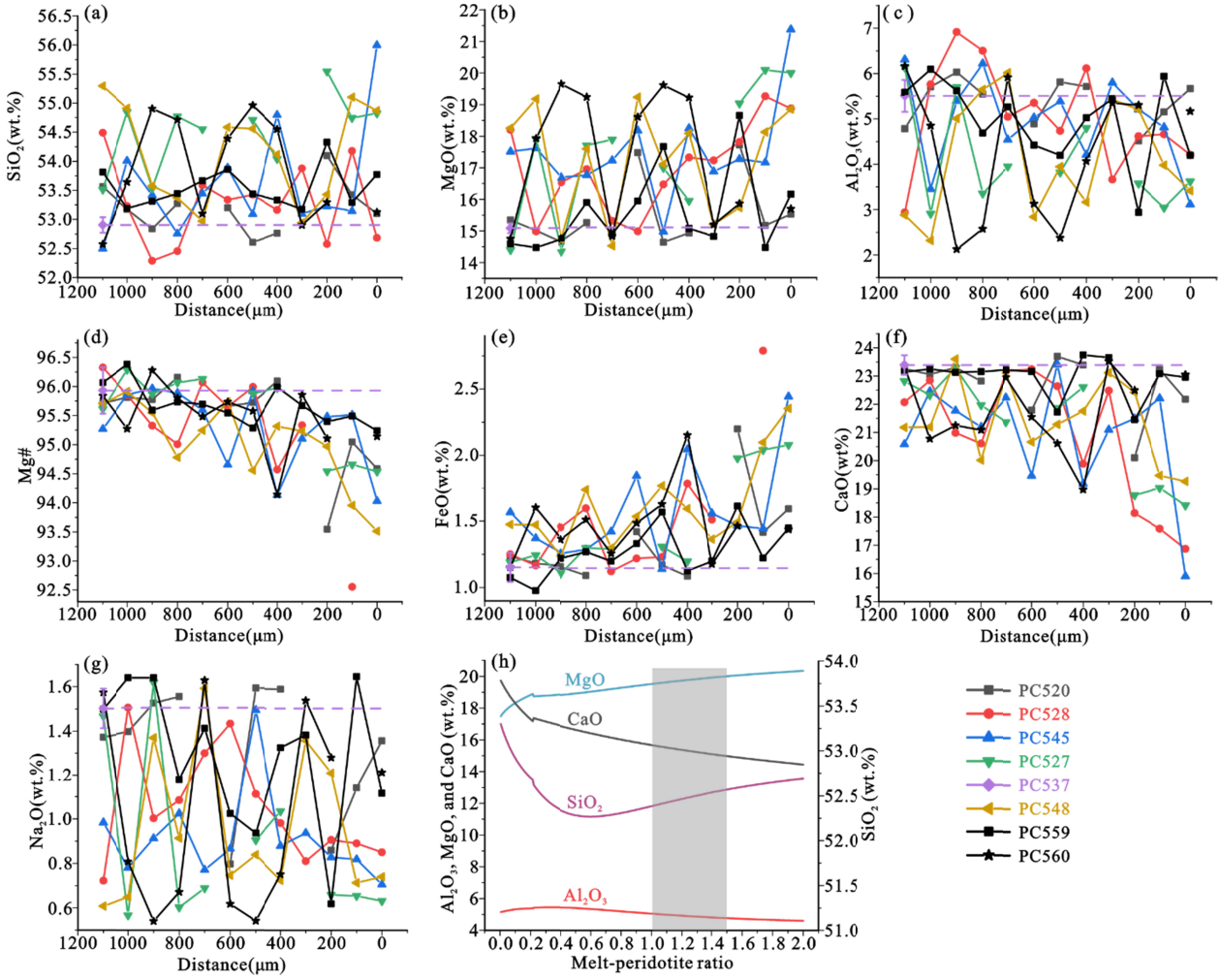

Figure 7. Plots (a-g) of measured oxide abundance (in wt.%) and Mg# in clinopyroxene as a function of distance (in μm) away from the melt-rock interface. The composition variations of

MgO, Al_2O_3, CaO, and SiO_2 are also simulated thermodynamically as a function of the melt-peridotite ratio in (h). The legends are the same as in Figure 6.

3.2.2 Silicate melt and sulfide liquid compositions

The evolution of the reacted melt composition in these layered experiments mostly depends on the extent of melt-rock reaction and the major phase formed by the reaction. In the melt source, with increasing run time and/or temperature, the compositions of silicate melt became higher in CaO and MgO concentrations, and lower in SiO_2, Al_2O_3, and FeO (Figure 8), implying the effect of high-degree melt-peridotite reaction on the melt composition. No distinct variation of the melt sulfur contents was observed under the conditions of 1250 ℃ and 1.5 GPa (Figure 8f), potentially indicative of sulfur-saturated silicate melt in these experiments. The decrease of pressure and temperature respectively to 0.5 GPa and 1200 ℃ caused the obvious increases in SiO_2 and Al_2O_3 concentrations and a slight decrease of S concentration in silicate melt. In addition, no significant variations of melt compositions were observed between the melt source and melt-peridotite interface within the error of measurement (Figure 8), suggesting the convective flow is strong enough to drive the chemical equilibrium of silicate melt. The composition of primary silicate melt infiltrating into the peridotite cannot be analyzed due to the small scale. In addition, ~ 1.57 ± 0.15 wt.% H_2O was detected in the reacted melts from experiment PC520 and PC528 using the Fourier Transform Infrared Microscopy (Supporting Information, Mercier et al., 2010), which is slightly higher than that of basalt (~ 1.19 wt.%) added in the starting materials.

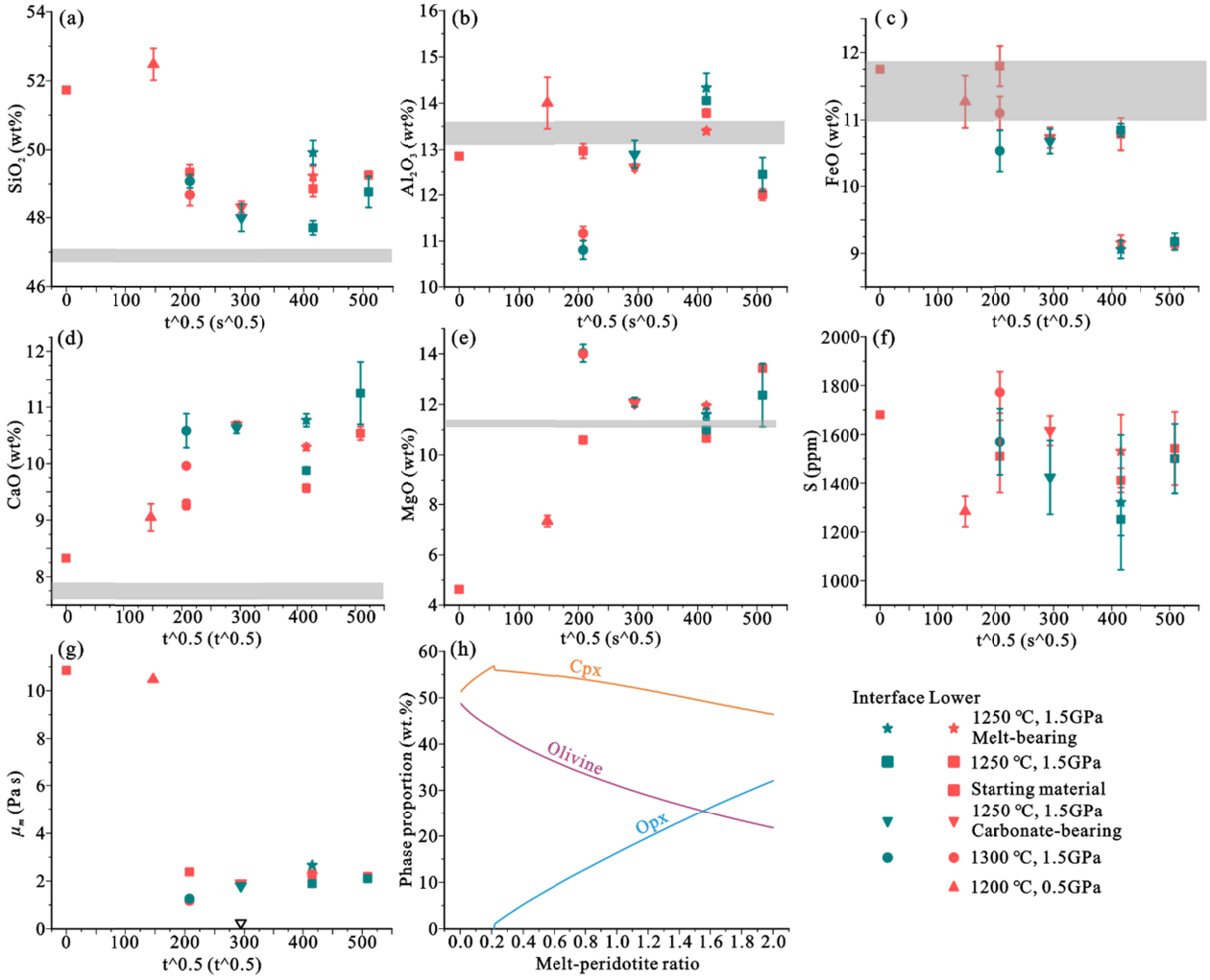

Figure 8. Plots of oxide abundance (in wt.%) (a-e), sulfur content (f), and viscosity (μ_m) (g) of silicate melt versus run time in melt-rock interface and lower melt source of these reaction experiments. The ranges of composition variations of SiO_2, Al_2O_3, FeO, CaO, and MgO simulated thermodynamically are denoted as gray shadow regions in (a)-(e) when the melt-peridotite ratio varies from 1 to 1.5. Produced phase proportions of different silicate minerals during the melt-rock reaction are also simulated thermodynamically as a function of melt-peridotite ratio in (h). A lower melt viscosity (~ 0.25 Pa s) of carbonate-bearing experiment (PC560) is roughly estimated using a simple model from Di Genova et al. (2014) and denoted as a hollow inverted triangle in (g). Cpx-clinopyroxene, Opx-orthopyroxene.

Except for several large sulfide droplets containing the Ni-rich quenched phases, the composition of sulfide was homogeneous in the lower melt source of all experiments. In the 12h experiment, the S content, Ni/S and Fe/S ratios of sulfide liquid were ~ 35.16 ± 0.72 wt.%, ~

0.39 ± 0.03, and ~ 1.43 ± 0.04, respectively, and these values (S ~ 35.74 ± 0.74 wt.%, Ni/S ~ 0.37 ± 0.09, Fe/S ~ 1.42 ± 0.06) remained constant within the error of measurement when the annealing time increases to 72h. However, the Cu/S ratio of sulfide liquid slightly decreased from 0.017 ± 0.004 at the 12h to 0.009 ± 0.002 at the 72h at 1250 ℃, while an obvious increase in the Cu/S ratio (~ 0.046 ± 0.010) was observed at 1300 ℃.

4 Discussion

4.1 Grain-scale processes in melt-peridotite reaction

Firstly, based on the thermodynamic model via the pMELTS (Ghiorso et al., 2002), if the upper peridotite reaches equilibrium at 1.5 GPa and 1250-1300 ℃, the corresponding melt fraction is less than 0.04-0.08 wt.%, implying that the self-partial melting of peridotite at the experimental conditions here is negligible. Therefore, the observed variations of melt area fraction, phase proportions, and minerals' sizes and compositions in the experimental products are likely to be due primarily to the melt-peridotite reaction. On the other hand, the upper peridotites are not in equilibrium with the starting lower melts at the experimental conditions, and hence olivine and clinopyroxene in the peridotite part will partially or completely dissolve in the reacting and upward percolating melt (Liang, 1999; C. Wang et al., 2020). In multicomponent partially molten systems, the melt-peridotite reaction is widely suggested to occur via multi-scale mass transfer processes that inevitably involve both the grain-scale dissolution-precipitation-reprecipitation and diffusion, in conjunction with large-scale advective transport (Cascio et al., 2008; Morgan & Liang, 2005).

In our high-temperature, high-pressure experiments (1.5 GPa and 1250-1300 ℃) here, due to the disequilibrium between melt and peridotite, the consequent grain-scale processes can mostly occur via the dissolution, precipitation, and reprecipitation of mineral grains, which is evident from the formation of ORL. In the lower melt source, the basaltic melt in starting materials is olivine-undersaturated, and thus the melt-rock reaction between basaltic melt and olivine produces new Opx grains (Figure 1), which is consistent with the following reaction:

$$melt_0 + Ol_0 \longrightarrow melt_1 + Opx_1, \quad (1)$$

where subscripts 0 and 1 designate melt and mineral grains from starting materials and the reaction products, respectively. This reaction should occur via the dissolution of olivine, and

precipitation of new orthopyroxene, largely contributing to the formation of ORL in the interface between the peridotite and melt source (Figure 1a). It is well known that dissolution and precipitation occur simultaneously during the development of the ORL under high pressure (> 1 GPa) (Cascio et al., 2008; Morgan & Liang, 2003). With increasing the degree of melt-peridotite reaction (a longer run duration and/or higher temperature), the olivine-melt layer above the ORL is formed by the further dissolution of olivine and few clinopyroxene grains, with concomitant reprecipitation of fresh olivine grains during melt reaction flow (Figure 2) (Kelemen et al., 1995).

On the other hand, the grain size of silicate minerals is a vital role in affecting the physical properties of upper partially molten peridotite, such as permeability (Faul, 2001). Here, the growth of silicate mineral sizes in the upper partially molten peridotite with increasing annealing time (Figure 4b) is mainly driven by a reduction of grain boundary energy (Faul & Scott, 2006) and demonstrates that textural coarsening by which small size grains are consumed as supply material for the growth of coarser grains (Higgins, 1998, 2011; Yao et al., 2017), may overweigh the decreasing-size effect driven by the reprecipitation of new, fine-grained crystals. The transference of material from dissolved olivine to other grains can occur via diffusion through crystals themselves, grain boundaries, and the interstitial melt (Yao et al., 2017), while the last one is much faster and becomes the main pathway of these grain-scales processes. Finally, the large-scale advective transport of the reacting melt is also evident from the variations of melt area fraction in the partially molten peridotite and the formations of melt junctions and channels (Figure 1; Figure 4a).

Based on the parabolic law of diffusive dissolution (Liang, 1999; Zhang et al., 1989), the slope (*i.e.*, the diffusive dissolution constant) of the fitted linear regression line for our experiments is used to estimate the growth rate of ORL (k_{ORL}), which is about ~ 0.78 ± 0.05 μm/s$^{0.5}$ here at 1.5 GPa and 1250 °C and far lower than those of some previous experiments conducted under higher temperatures and/or pressures (Figure 3a) (Morgan & Liang, 2005; C. Wang et al., 2020). However, the thickness of ORL in experiment PC527 at 1.5 GPa and 1300 °C has a faster-increasing tendency (k_{ORL} = 2.37 ± 0.14 μm/s$^{0.5}$), consistent with the experiments under 2 GPa and 1375 °C (C. Wang et al., 2020). This tendency of ORL growth is likely unchanged in the experiments with the carbonate-bearing melt source (PC560) and silicate melt-bearing peridotite (PC548) (Figure 3a), implying an insignificant effect of the melt composition

and the porosity on the growth of ORL in these experiments. These results indicate that the increases in temperature and pressure will potentially enhance the growth rate of the ORL thickness during the melt-rock reaction, which can be mostly attributed to the higher diffusivities of elements in silicate melt at a higher temperature (Mungall, 2002; Zhang et al., 2010).

Similarly, we observed the linear increase of dissolution distance with the square root of time (Figure 3b), suggesting that a substantial amount of peridotite was dissolved in the percolating melt. At 1.5 GPa and 1250 ℃, the dissolution rate of peridotite evaluated by the slope of the linear regression line (k_{diss} = 0.58 ± 0.08 μm/s$^{0.5}$) is lower than those in previous experiments with higher temperatures and pressures (Figure 3b, C. Wang et al., 2013, 2020), indicating that relatively high temperature and pressure could also increase the dissolution rate. Moreover, the higher dissolution rate of peridotite at experiment PC527 (1300 ℃) implies that the increase in temperature significantly enhances the melt-rock reaction (Mitchell & Grove, 2016). The high content of water (~ 1.57 ± 0.15 wt.%) in silicate melt could also enhance the formation of several enormous Opx grains in the ORL (Figure 2) (Wang et al., 2016), partly because the addition of water can strongly depress the peridotite solidus. This may be also the reason for the large standard deviations of the dissolution rate in experiment PC527 and PC545 with high temperature (1300 ℃) and long annealing time (72h). Overall, the growth rate of the ORL is generally higher than the peridotite dissolution rate, which is partly due to the growth of ORL not only involves the precipitation of some new mineral grains in the process of melt-enhanced dissolution of peridotite, but also is produced by the volume-increasing reaction during the replacement of olivine by orthopyroxene (Milke et al., 2009).

4.2 Compositional variations of melt and minerals

During the melt-peridotite reaction, besides the systematic changes in mineralogy and texture of peridotite, we also observed the compositional variations of melt and minerals in the reaction couple (Figure 6-8), which have been widely used to outline the grain-scale processes governing this melt-peridotite reaction (Mallik & Dasgupta, 2012; C. Wang et al., 2020). On the other hand, a thermodynamically-constrained mixing model has been recently adopted to examine the variations of major element compositions during the melt-peridotite interaction (Lambart et al., 2012; Pin et al., 2022; Shaw et al., 2018), and this forward model may offer a key to testing and understanding the compositional evolution of our experimental products.

In this regard, the melt-peridotite reaction is modeled as a simplified, thermodynamic process in which the peridotite is continually impregnated by a finite amount of basaltic melt from the lower melt source, which is the same as the assumption in previous works (Lambart et al., 2012; Pin et al., 2022; Shaw et al., 2018). Once each increment of melt impregnation, the infiltrated melt will eventually be equilibrated with the surrounding peridotite, and the thermodynamic properties of the whole system should be adopted as a reference for the next increment. In each increment, the proportions and compositions of melt and solid phases after the chemical re-equilibrium can be modeled by minimizing the Gibbs energy of the whole system from constraints on bulk composition, temperature, pressure, enthalpy, and oxygen fugacity (Pin et al., 2022; Yao et al., 2018). This process is simulated by constantly adding up to 200 g of the lower basaltic melt by increments of 0.5 g, to 100 g of the upper peridotite, using the pMELTS of alphaMELTS (Ghiorso et al., 2002; Ghiorso & Sack, 1995; Smith & Asimow, 2005) in isenthalpic mode at 1.5 GPa, 1250-1300 °C and ΔQFM-2.0. Here, the incremental addition of basaltic melt corresponds to the increase of melt: peridotite ratio from 0.005 to 2.

Our simulation shows that the mass fraction of olivine decreases from ~ 49 wt.% to ~ 21.8 wt.% with the increasing melt: peridotite ratio from 0.005 to 2 (Figure 8h). The silicate melt becomes saturated with orthopyroxene when the melt: peridotite ratio reaches a value of ~ 0.22. After this point, the mass fraction of new orthopyroxene precipitated from silicate melt quickly increases to ~ 32 wt.% at the melt: peridotite ratio of 2 (Figure 8h). In contrast to the initial peridotite, the mass fraction of clinopyroxene has a quick increase from ~ 51 wt.% to ~ 57 wt.% before the precipitation of orthopyroxene, but then slowly decreases to ~ 46 wt.% at melt: peridotite ratio = 2 (Figure 8h). Hence, the increase in orthopyroxene proportion is mostly due to the dissolution of olivine, accompanied by a limited contribution from the consumption of no more than ~ 5 wt.% clinopyroxene, which approximatively coincides with the hypothetical Reaction 1 mentioned above.

Concurrently, the melt penetrates upwards and further reacts with the peridotite to result in systematic variations of the compositions of olivine and Cpx grains towards the melt-rock interface (Figure 6 and Figure 7). The modeled compositional evolutions of olivine show decreasing trends of MgO and SiO_2 contents respectively from ~ 49.3 wt.% to ~ 44.1 wt.% and 40.9 wt.% to 39.7 wt.%, an increase of FeO content from ~ 9.0 to ~ 14.5 wt.%, and the associated decrease of Mg# from ~ 90.7 to ~ 84.4, when the melt: peridotite ratio increases from

~ 0.005 to ~ 1.5 (Figure 6h). In the same range of melt: peridotite ratio, the clinopyroxene has an obvious increase in its MgO content (from ~ 17.5 to ~ 20.0 wt.%) and approximately constant SiO_2 and Al_2O_3 contents (Figure 7h). The trends of these compositional variations of minerals are nearly in agreement with those of our experimental measurements, except for the low-pressure experiment (PC 559, Figure 6h and Figure 7h). Therefore, the measured compositional variations of olivine and clinopyroxene as a function of distance away from the final melt-peridotite interface may be referred to the melt: peridotite ratio at any position of the upper peridotite. The measured compositions of olivine and Cpx grains just above the final melt-peridotite interface are approximately consistent with those results simulated thermodynamically (Figure 6h and 7h gray shadow regions) in the range of melt-peridotite ratio of 1.0 to 1.5, which suggests that they have obtained locally chemical re-equilibrium with the reacting melt that is about ~ 1.0-1.5 times the initial mass of peridotite in the same region. As the distance away from the final melt-peridotite interface grows, the increasing MgO and Mg# of olivine reflect the decrease of melt: peridotite ratio, and consequently imply the gradual weakening of melt-peridotite reaction. Hence, when the upward-flowing melt encounters the partially molten peridotite that initially has a low permeability, strong convection and backflow of silicate melt and the associated high-degree melt-peridotite reaction mostly occur at the bottom of peridotite and thus lead to an increase of porosity of the reaction region and a larger buoyancy-driven upward motivation of silicate melt, which produces positive feedback between the reaction and melt flow contributing to the upward infiltration of more silicate melt into the partially molten peridotite.

Along with the increasing melt: peridotite ratio from ~ 1.0 to ~ 1.5, the modeled silicate melt that is reacted with the peridotite shows a decrease of SiO_2 content from ~ 47.1 wt.% to ~ 46.7 wt.%, which is similar to the measured ranges in our experiments with long annealing time but has a slightly lower SiO_2 content at high melt-peridotite ratio (Figure 8a). The Al_2O_3 content of silicate melt also varies from ~ 13.6 wt.% to ~ 13.1 wt.%, while the MgO content of melt shows a narrow variation range of ~11.1 to ~11.4 wt.%, which both roughly match those results measured in this study (Figure 8b and e). The possible iron loss to Pt capsule in these experiments due to the incomplete isolation of separate upper and lower graphite capsules with different diameters for silicate melt from Pt capsule (J. Wang et al., 2020) is likely to be the main reason for the lower FeO content (Figure 8c) measured in those experiments with long annealing

time (> 48h). The model suggests that silicate melt contains ~ 7.6-7.9 wt.% CaO at the melt-peridotite of 1.0-1.5, but this range is largely underestimated in contrast to our measurements (Figure 8d), partly because the slight differences in the Gibbs free energy among various compositional models of pyroxenes (Yao et al., 2021) may drive large errors in the CaO content of clinopyroxene in the AlphaMELTS. Although there still have some weaknesses in modeling the compositional evolution of silicate melt, the use of AlphaMELTS is encouraging here, and helps to examine how mineral model and chemical composition evolve as silicate melts are added into the peridotite part.

4.3 Coarsening processes of sulfide droplets

In a partially molten system, the nucleation/growth rate and associated size distribution of sulfide droplets are vital constraints on their dynamics (Yoshino & Watson, 2005). Along with the increasing annealing time, the size of sulfide droplets shows a larger increase (from ~3.2 ± 0.1 μm to ~11.1 ± 0.4 μm) (Figure 5c) compared with that (from ~8.1 ± 3.4 μm to ~11.0 ± 4.9 μm) (Figure 4b) of the surrounding silicate minerals. The growth of silicate minerals has been suggested to be mostly controlled by the melt-enhanced diffusion of material, but sulfur that is the one of major elements in the sulfide has a much lower diffusivity than those of other elements (Freda et al., 2005; Yao & Mungall, 2021). Given that S diffusion rather than Fe diffusion limits the growth rate of sulfide droplets (Zhang, 2015), if the growth of droplets completely occurred via the diffusion of S, it should have a smaller growth rate than that of silicate minerals, which is opposite to our measurements. Therefore, besides the diffusion-driven growth, there must be other mechanisms here contributing to the fast growth of sulfide droplets.

On the other hand, the actual 3D size distribution of sulfide droplets in the melt source shows a uniform, nearly log-normal size distribution independent of annealing times with a skewed peak to a slightly smaller size than the average one (Figure 9), which can be attributed to the possible contribution of the Lifshitz-Slyozov-Wagner (LSW) coarsening and the occurrence of normal grain growth (Honour et al., 2019; Yoshino & Watson, 2005).

Based on the classical LSW theory (Lifshitz & Slyozov, 1961; Wagner, 1961), the kinetics of particle growth can be approximately described as $r \sim t^{1/m}$, where r is the grain size, with the exponent $m = 3$ for a diffusion-controlled process and $m = 2$ under the control of an interface reaction. At 1250 ℃ and 1.5 GPa, coarsening rates of sulfide droplets are slightly

slower than that predicted (m = 2) by the interface-reaction-controlled process due to a transient regime ripening before static-state ripening (Figure 5a), implying the likely combination of multiple coarsening processes here (Lautze et al., 2011; Sun, 2007). The higher run temperature (1300 ℃) likely contributes to a higher degree of interface-controlled reaction (Yoshino & Watson, 2005), which can potentially facilitate the coarsening processes of sulfide liquid in the melt source (Figure 5a). A dramatical decrease in the number density of sulfide droplets (Figure 5a-inset) and the presence of sulfide droplets in contact with each other (Figure 2b and Figure S1) in the melt source both imply that the contribution of mechanical coalescence of sulfide droplets (agglomeration and successive coalescence) to their coarsening processes may be more important at droplet contacts (Yoshino & Watson, 2005). Moreover, silicate melt structure strongly affects the tendency of sulfide droplets to coalesce, and the coalescence of sulfide droplets could be enhanced at lower viscous melts (Holzheid, 2010), potentially addressing a significant increase in the coarsening rate (Figure 5a) in the carbonate-bearing experiment (PC560) with a lower melt viscosity (Figure 8g) (Di Genova et al., 2014). Although the previous analog experiment (de Bremond d'Ars et al., 2001) and some static high-temperature and high-pressure experiments (Bockrath et al., 2004; Holzheid, 2010) did not observe significant coalescence of sulfide droplets, the mechanical coalescence of sulfide droplets, for the first time, has been demonstrated to be feasible in our experiments with strong melt convection and melt-peridotite reaction. This mechanical coalescence process may potentially occur via the impaction of sulfide droplets with each other, and drainage and rupture of the infinitesimally liquid film separating them during the reacting melt flow, as suggested by theoretical analyses (Yao et al., 2019).

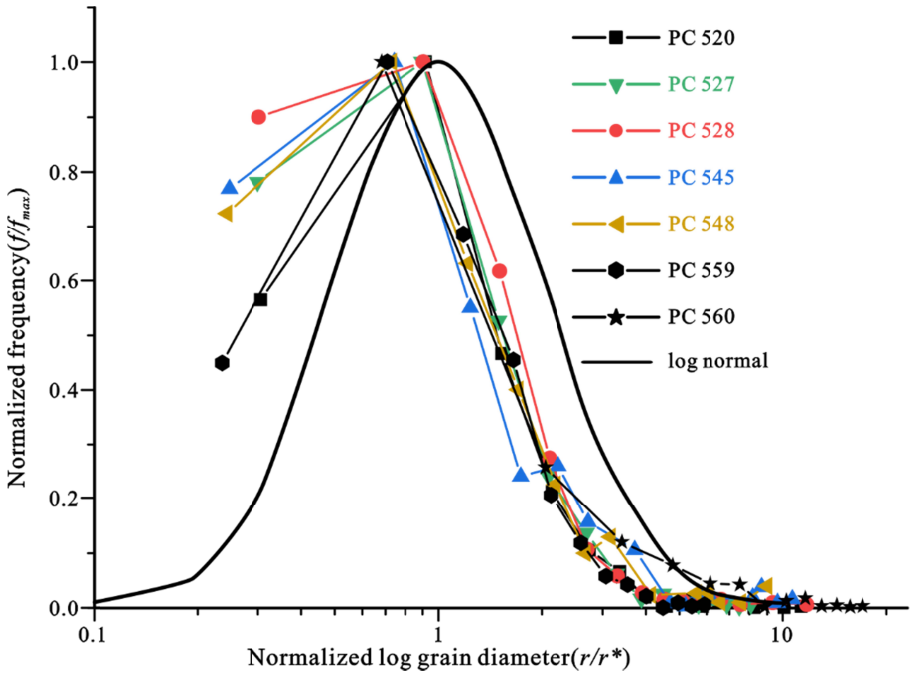

Figure 9. Normalized 3D size distributions of sulfide droplets in the melt source. The size of sulfide droplets (r) and frequency (f) are normalized to average size (r*) and maximum frequency (f_{max}), respectively.

4.4 Dynamics of melt flow and entrainment of fine sulfide droplets

These dissolution-reprecipitation processes not only change the composition and proportion of solid phases, but also increase the porosity of peridotite in the upper part of samples, thereby enhancing the upward mobilities of silicate melt and sulfide droplets away from the lower melt source (Figure 4). Moreover, the porosity of ORL is enough high for the entrainment of sulfide droplets into peridotite (Figure 1 and Figure 2). In addition, with increasing annealing time to 72h, more basaltic melt infiltrating into the peridotite region from the melt source (Figure 4) could potentially enhance the reaction between basalt melt and peridotite. Melt-rock reaction may produce a high flow capacity of reacting melt through a dissolvable peridotite (Chadam et al., 1986; Jackson et al., 2018), resulting in the formation of finger- or tree-like melt-rich channels in which a fast-ascending magma flow can even drive the antigravitational migration of some coarse olivine grains (Pec et al., 2017). Hence, the development of positive feedback between the permeability due to the melt-peridotite reaction and the associated increase of melt flux in reacting regions produces a higher flow velocity of

591 melt and wider melt channels among crystal framework (Aharonov, 1995; Pec et al., 2017),
592 thereby potentially facilitating the upward entrainment of sulfide droplets (Wang & Jin, 2020).

593 To quantitatively outline the upward physical migration of sulfide droplets along with the
594 reactive melt flows in the dissolvable peridotite, some theoretical parameters of physical
595 properties of the partially molten rock should be considered first (*e.g.*, von Bargen & Waff,
596 1986; Mckenzie, 1984). For an ideal porous crystal framework, the permeability (k) can be cast
597 by using a simple power-law relationship between grain size (d) and porosity (Φ) of the crystal
598 matrix (von Bargen & Waff, 1986):

599 $$k=\frac{\Phi^n d^2}{C}, \quad (2)$$

600 where C and n are constant parameters depending on the topology of melt phase and the
601 geometry of an individual melt channel. Based on the previous works (Miller et al., 2014; Z.
602 Wang et al., 2020), here some suitable ranges of C (36-94) and n (2.4-2.8) are adopted for our
603 experiments that contain the multiphase-mineral assemblage.

604 On the basis of the numerical model from McKenzie (1989), the extraction velocity of
605 melt relative to the stationary crystal framework can be estimated by:

606 $$v=\frac{k\Delta\rho_m g}{\Phi\mu_m}, \quad (3)$$

607 where $\Delta\rho_m$ - the density contrast between silicate melt and solid mineral, g - the gravitational
608 acceleration, and μ_m - the melt viscosity, which decreases with increasing temperature and
609 volatile content (mainly CO_2 and H_2O) (Dingwell, 1996; Di Genova et al., 2014). Due to the
610 models from Giordano et al. (2008), the viscosity (μ_m) of the starting basalt can be calculated as
611 ~ 10.8 Pa·s at 1250 °C, whereas the μ_m of reacting melt after melt-rock reaction decreases to ~
612 1.2-2.7 Pa·s under conditions of 1.5 GPa and 1250-1300 °C (Figure 8g). The reactive melt has a
613 higher viscosity of ~10.5 Pa·s when the pressure and temperature respectively decrease to 0.5
614 GPa and 1200 °C (Figure 8g). Based on equation (2) and (3), the porous flow velocity of melt
615 through grain-scale percolation is ~ 0.76 μm/h in the partially molten peridotite of experiment
616 PC545 (Φ ~ 7.13 %; μ_m ~ 2.2 Pa s; d ~ 11.0 μm; C ~ 36, n ~ 2.6, Miller et al., 2014; $\Delta\rho_m$ ~ 600
617 kg/m^3). Apparently, the transport distance (~ 54.7 μm) of this slow-extracting (~ 0.76 μm/h) melt
618 within the longest experimental time (72h) is much shorter than the region of melt-peridotite

reaction observed in experiments (Figure 1a), which implies that other mechanisms of melt extraction occur concurrently to drive a higher flow velocity. In addition to the melt junctions among minerals, we also observed thick melt channels (Figure 2) between some opening mineral grain boundaries in the ORL and olivine + melt layer where a new crystal framework may have not been built, indicating the possible contribution of melt channel flow, which have been demonstrated by some experimental studies (*e.g.*, Pec et al., 2017; Zhu et al., 2011) and the field investigations on dunite channels in MORB (*e.g.*, Kelemen et al., 1995). The melt velocity in these channels is suggested to be much higher relative to other regions (Pec et al., 2017; Wang & Jin, 2020).

The physical mobility of sulfide liquids along with the sulfur-saturated silicate melt within the crystal framework of partially molten peridotite largely depends on the size of sulfide droplets, the permeability of crystal framework, the connectivity of melt network, and the processing degree of melt-rock reaction (Z. Wang et al., 2020; Yao & Mungall, 2020). Chung & Mungall (2009) has simplified this complex process and proposed that the migration of sulfide is mostly controlled by the relative sizes of sulfide droplets and surrounding crystals within partially molten peridotite. When a sulfide droplet is smaller than the size of the most constricted part of melt channel or pore throat in the crystal framework, it can be easily entrained by ascending melt through peridotite without any obstruction if the terminal settling velocity of sulfide droplets is less than the upward velocity of melt flow. For the spherical sulfide droplet, the terminal settling velocity will achieve when its gravity-driven buoyancy force (F_B) can be balanced by the vertical drag force (F_D).

The melt flows passing through sulfide droplets that are nearly stranded in the melt channels or port throat, as a first approximation, can be regarded as the flow of a viscous incompressible fluid around a circular cylindrical post (*i.e.*, the sulfide droplet) confined between two parallel flat plates (*i.e.*, the melt channel) (Figure 10a) (Lee & Fung, 1969). The drag force (F_D) acting on this sulfide droplet can be expressed by a dimensionless coefficient (f_D):

$$F_D = f_D \times 4\pi\mu_m UR, \tag{4}$$

where R is half the distance between the two plates, *i.e.*, the radius of the melt channel, and U is the stokes flow velocity of melt around sulfide droplet. Based on the modeling results from Lee & Fung (1969), this dimensionless coefficient, f_D, can be estimated via the ratio between R and r_s

649 that is the radius of an initial undeformed sulfide droplet before entering the melt channel (Figure
650 10b). For simplification, here we assume that spherical sulfide droplets have a radius (r_s)
651 equaling to or being slightly higher than R, and thus the corresponding values of f_D should
652 exceed ~ 4.8 (Figure 10b) (Lee & Fung, 1969).

653 On the other hand, sulfide droplets always have a trend of settling to the base of the
654 capsule due to gravity, and the corresponding buoyancy force (F_B) can be expressed as:

655 $$F_B = \frac{4}{3}\pi r_s^3 g \Delta\rho_s, \quad (5)$$

656 where $\Delta\rho_s$ = 1700 kg/m^3 is the density difference between the sulfide and silicate melt (Kress et
657 al., 2008; Z. Wang et al., 2020). Hence, constrained by fluid dynamical arguments, the velocity
658 of melt flow that just successfully entrains sulfide droplets whose sizes are close to that of melt
659 channel/pore throat can be calculated via:

660 $$U = \frac{F_D}{4\pi\mu_m R \cdot f_D} = \frac{F_B}{4\pi\mu_m R \cdot f_D} = \frac{r_s^3 g \Delta\rho_s}{3\mu_m R \cdot f_D}, \quad (6)$$

661 Because the measured maximum radius of sulfide droplets in the upper peridotite part is
662 ~ 9.5 μm under the conditions of 72h and 1250 °C, the maximum value of U can be estimated as
663 about ~ 170.9 μm/h (~ 1.5 m/year), when the R/r_s equals to 1. This value, at least to some extent,
664 represents the localized velocity of channelized melt flow in the regions of melt-rock reaction
665 and is nearly three orders of magnitude higher than the velocity of melt porous flow (~ 0.76
666 μm/h) driven by the compaction of dense crystal framework. Given the velocity of melt flow
667 should be changeable due to the complex morphology of interconnected melt channels and
668 variable fluid dynamic environments in porous peridotite (McKenzie, 1989; Miller et al., 2014;
669 Z. Wang et al., 2020; Zhu et al., 2011), our calculation (~ 1.5 m/year) here can be used as an
670 order of magnitude estimate for the velocity of melt flow around sulfide droplet through narrow
671 pore throat in these experiments.

672 First of all, we must use some reasonable geometrical parameters of the natural partially
673 molten rocks, such as the grain size, and the distribution of relative sizes of pores and pore
674 throats (Chung & Mungall, 2009; Yao & Mungall, 2020), before extrapolating our models to the
675 partially molten mantle. Commonly, the porosity (Φ) is approximately estimated to be ~ 1-15 %
676 in the partially molten mantle (*e.g.*, Mei et al., 2002; Yoshino et al., 2010; Zhu et al., 2011), and
677 the high-degree melt-rock reaction regions would be expected to obtain a higher porosity (Pec et

al., 2017). Thus, the Φ in melt-rock reaction regions is properly set as 3-20 % in this study. The observed grain size of upper mantle peridotite is about mm-scale (Ave Lallemant et al., 1980; Karato, 1984), and thus the crystal radius (R_c) could be reasonably set as ~ 1.5 mm, which is about two orders of magnitude higher than the grain size (~ 10 μm) in our experiments. Hence, the permeability of upper mantle peridotite is much higher than the estimated value for our experiments, and consequently, the extraction velocity of melt relative to the stationary crystal framework could even increase from about ~ 4.88×10^{-6} – 5.73×10^{-5} m/s (~ 153.89 – 1807.20 m/year) with the growth of Φ from 3 to 20 %, if other parameters in equation (3) remain constant.

On the other hand, for the partially molten mantle, a diversity of properties and mechanisms contribute to the heterogeneous physics of melt extraction (Katz et al., 2022; Z. Wang et al., 2020; Zhu et al., 2011), and the melt transport velocities can be estimated to be a wide range of 1 to 1000 m/year by analyses of uranium-series (U-series) disequilibria in lavas and Icelandic deglaciation (Katz et al., 2022; Rees Jones & Rudge, 2020; Rubin et al., 2005). Commonly, channelized melt flow potentially characterizes a high melt extraction velocity in melt channels with high porosity, which could even reach ~ 10 km/year (McKenzie, 2000). In contrast, recent laboratory experiments further estimate some lower velocities (~ 2.4-29.7 m/year, Z. Wang et al., 2020; ~ 2-150 m/year, Connolly et al., 2009; ~ 0.5 m/year, Zhu et al., 2011). Obviously, these above values (~ 0.5-10000 m/year) are orders of magnitude almost the same as or significantly larger than those (~ 153.89 – 1807.20 m/year) of our experiments, and the high estimated value could be attributed to the heterogeneous melt flow, the larger grain size and associated higher permeability in the natural peridotite than those in our experiments.

Combined with the numerical model from Sweeney & Martin (2003) estimating the relationship between the R/R_c ratio and Φ, we depict the radius (r_s) of initial undeformed sulfide droplet that can pass through the pore throat as a function of Φ of the partially molten mantle in Figure 11. When the radius (r_s) of a sulfide droplet is smaller than and equal to the minimum constriction (R) of the melt channel, the relationship between r_s and Φ is displayed in the regions of No. 1 and 2 of Figure 11. If the flow velocity is less than ~ 1.16×10^{-5} m/s (about 366 m/year), the vertical drag force (F_D) from this slow-flowing melt starts to be smaller than the gravity-driven buoyancy force (F_B) of sulfide droplet that has the same or similar radius with that of pore throat at high porosity. In this situation, the maximum size (~ 148.5 μm) of upward migrating sulfide droplet is limited by the low flow velocity and will keep constant at high porosity, but is

still controlled by the radius of pore throat at low porosity. Assuming that the velocity of the melt flow increases from about 5.1×10^{-6} m/s (~ 160 m/year) to 2.1×10^{-5} m/s (~ 660 m/year), the maximum radius of sulfide droplets that could be carried along with silicate melt increases from about ~ 98.2 μm to ~ 200.0 μm (Figure 11-No. 1 region), and with increasing Φ to 20%, the value of r_s significantly increases up to 246.7 μm, which is equal to the radius of pore throat at Φ = 20%, with a lower limit of velocity ~ 3.2×10^{-5} m/s (~ 1010 m/year) (Figure 11-No. 2 region). These indicate that the size of sulfide droplets is dominated by the grain size and porosity of peridotite, that is the size of pore throat, and the velocity of melt porous flow under the condition of $r_s \leq R$.

Therefore, during the melt-peridotite reaction, the accompanying melt flow in the dissolved peridotite is energetic, and its flow velocity seems to be high enough to drive the upward transport of fine μm-scale sulfide droplets (Figure 10c-right side; Figure 11-the No. 1 and 2 regions).

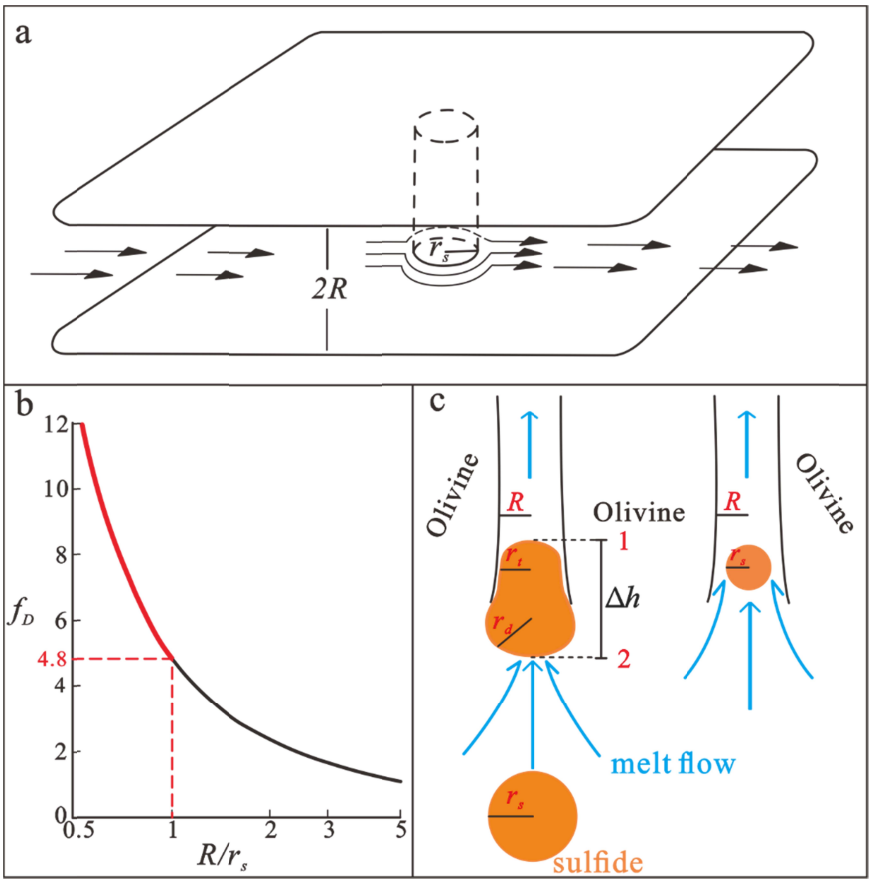

723 **Figure 10**. Schematic map illustrating the flow of a viscous incompressible fluid around a
724 circular cylindrical post confined between two parallel flat plates (a), the dimensionless
725 coefficients f_D representing the drag force acting on sulfide droplet as a function of the R/r_s ratio
726 (b) (modified from Lee & Fung, 1969), and the extrusion and entrainment of large (left side) and
727 small (right side) sulfide droplets driven by focused melt flow (c). In (a), the two parallel flat
728 plates and a circular cylindrical post are considered as the walls of the pore throat/melt channel
729 and sulfide droplet, respectively.

730 **4.5 Potentially upward transport of coarse sulfide droplet**

731 When a coarse sulfide that is sufficiently larger than the minimum constriction of the
732 melt channel is gradually squeezed into the small "throat" part along with the ascending reactive
733 melt flow, the sulfide droplet will invade this throat and be deformed into a pear shape with a
734 smaller radius of curvature (Figure 10c-left side). Obviously, the upward migration of this coarse
735 sulfide droplet in the partially molten peridotite becomes complicated, and the associated
736 dynamic process can simplistically involve a competition between pressure gradient, viscous,
737 buoyancy, capillary, and drag forces (Yao & Mungall, 2020). This squeezing process introduces
738 the additional capillary pressure P_c, which is a measure of the pressure discontinuity existing at
739 the interface of two immiscible phases (Chung & Mungall, 2009). The additional pressure
740 imposed on this deformed sulfide droplet within the squeezing process equals the difference in
741 capillary pressure between the top and bottom interfaces of the sulfide droplet and can be
742 calculated by:

743 $$\Delta P_c = 2\gamma_{ms} \times \left(\frac{1}{r_t} - \frac{1}{r_d}\right), \quad (7)$$

744 where γ_{ms} = 0.21 N/m is the melt-sulfide surface tension (Mungall et al., 2015), r_t is the radius of
745 the upper spheric cap, and r_d is the radius of the lower part of the pear-shaped droplet (Figure
746 10c). The droplet cannot be forced through the pore throat unless this excess pressure ΔP_c is
747 balanced by an equal or greater pressure (ΔP) exerted by the ascending melt flow on the trailing
748 edge of sulfide droplet, which tends to push the droplet to rise through the melt channel.

749 Because the silicate melt flows at low Mach number, the simple form of Bernoulli's
750 principle is valid for the quasi-incompressible flows in melt-peridotite reaction, and hence the

pressure of flowing melt around a sulfide droplet can be highly related to the peripheral flow velocity via the Bernoulli's equation (Bauman & Schwaneberg, 1994):

$$P_1 + \frac{\rho_m U_1^2}{2} + \rho_m g h_1 = P_2 + \frac{\rho_m U_2^2}{2} + \rho_m g h_2, \quad (8)$$

where the subscripts 1 and 2 correspond to the top and bottom outside points of deformed sulfide droplets along the axis of symmetry, respectively; P is the pressure caused by the flow of silicate melt; ρ_m is the density of melt; h is the height of 1 and 2 relative to a reference point beneath sulfide droplet. Hence, the flowing-melt-driven external pressure imposed on the deformed sulfide droplet equals the difference (ΔP) between P_1 and P_2. In an extreme case, the coarse, deformed sulfide droplet completely blocks the ascending melt flow, and the flow velocity at bottom of droplets (U_2) is close enough to zero, leading to the maximum value of external pressure difference (ΔP) that can be calculated as:

$$\Delta P = P_2 - P_1 = \frac{\rho_m U_1^2}{2} + \rho_m g(h_1 - h_2) = \frac{\rho_m U_1^2}{2} + \rho_m g \Delta h, \quad (9)$$

where U_1 is the flow velocity of melt at the top of sulfide droplet, and Δh is the vertical distance between the top and bottom points of the droplet. Assuming that the volume of a sulfide droplet is unchanged during the squeezing process, the height of this invading sulfide droplet (Δh) can be described by Chung & Mungall (2009):

$$\Delta h = r_t + r_d + \sqrt{r_d^2 - R^2} - \sqrt{r_t^2 - R^2}, \quad (10)$$

For the deformed sulfide droplet, it bears the upward pressure driven by flow melt (*i.e.*, ΔP), which should balance or even exceed the total of downward capillary pressure (ΔP_c) and gravity-driven pressure (P_G) for the droplet to rise through the constriction:

$$\Delta P \geq P_G + \Delta P_C = \rho_S g \Delta h + 2\gamma_{ms} \times \left(\frac{1}{r_t} - \frac{1}{r_d}\right), \quad (11)$$

where ρ_s is the density of sulfide liquid. Thus, combining the above equations (7-10), under the critical condition for migration of sulfide droplet into the pore throat to be the case ($r_t = R$) (Chung & Mungall, 2009), the equation 11 substituted with the appropriate values for ρ_m = 2600 kg/m^3 (Robertson et al., 2016) is simplified into:

$$1300 \times U_1^2 \geq 16660 \times \left(R + r_d + \sqrt{r_d^2 - R^2}\right) + 0.42 \times \left(\frac{1}{R} - \frac{1}{r_d}\right), \quad (12)$$

777 And finally, the initial radius (r_s) of this sulfide droplet before its invasion into the pore
778 throat can be calculated as Chung & Mungall (2009):

779 $$r_s = (0.5 \times (r_d^3 + R^3 + (r_d^2 + \frac{1}{2}R^2) \times \sqrt{r_d^2 - R^2}))^{1/3}, \quad (13)$$

780 When silicate melt flows around a sulfide droplet through a narrow pore throat in the
781 partially molten peridotite, the associated velocity field is suggested to be not homogeneous. In
782 addition, it is well known that exactly deciphering the flow velocity field of silicate melt
783 infiltrating through multi-mineral phase system plays a critically important role in understanding
784 geodynamic properties of the partially molten upper mantle, but it is really challenging and
785 beyond the scope of this study. The increases in grain size and permeability may also strongly
786 enhance the melt flow velocity in the new channel of crystal framework. Here, the flow velocity
787 in the channel has been confirmed to be about three orders of magnitude higher than that of
788 porous flow through grain-scale percolation, which may be extrapolated to the mm-scale upper
789 mantle peridotite. Therefore, the velocity of melt flow around a sulfide droplet in the channel in
790 upper mantle peridotite may be within the magnitude of 0.001-0.1 m/s, and thus the local
791 velocity (U_1) of focused melt flow around the top of sulfide droplet through the narrow pore
792 throat could be analogously assumed to be ~ 0.3 m/s and ~ 0.08 m/s here (Figure 11-No.3
793 region) as the possible values in the localized high-degree melt-rock reaction regions of the
794 partially molten mantle with high porosity. This range of flow velocity is also consistent with the
795 estimates from previous studies discussed in Section 4.4.

796 Equation 12 and 13 are numerically solved for the above value of U_1 by programming a
797 loop using Maple©. Based on the above numerical calculation, when the velocity of focused melt
798 flow around a sulfide droplet is within the range of ~ 0.08 m/s and 3.2×10^{-5} m/s (corresponding
799 to the range of the velocity of melt porous flow from ~ 2500 m/year to ~ 1 m/year), larger sulfide
800 droplets than the radius (R) of melt channel/pore throat are difficult to overcome the capillary
801 pressure and will be stranded in the inter-grain pores (Figure 11-region No. 3). However, these
802 flow velocities are still strong enough to drive the upward transport of sulfide droplets whose
803 radii are smaller than or similar to the radius (R) of pore throat, and as shown in the region of No.
804 3 of Figure 11, the estimated maximum value of r_s increases from ~ 100.9 to 247.3 μm at the
805 velocity of 0.08 m/s, which is roughly similar to R (from~ 99.7 to 246.7 μm in the region No. 2)
806 with the growth of Φ from 3 to 20 %. In this range of flow velocity, the maximum size of

807 upward migrating sulfide droplets is limited by the radius of pore throat and consequently
808 depends on the grain size and porosity of the upper mantle.

809 In contrast, for a powerful melt flow with extremely high velocity (*e.g.*, ~ 0.3 m/s in
810 Figure 11-region No. 3), coarse-grained sulfide droplet may overcome the capillary pressure
811 driven by the pore throat, and its maximum radius for upward migration increases from ~ 106.8
812 μm to ~ 276.8 μm with increasing the porosity from 3 % to 20 % (Figure 11-region No.3), where
813 the sulfide droplets can pass through pore throat narrower than themselves. Although the
814 estimates of the maximum sulfide size that are capable of upward migrating through the porous
815 molten peridotite are divided into three conditions, all of them are mostly dominated by the melt
816 flow velocity, porosity, and grain size of peridotite, which would be strongly enhanced by the
817 high-degree melt-rock reaction.

818 On the other hand, based on these previous studies on the abyssal and orogenic
819 peridotites, and peridotite xenoliths (Lorand & Luguet, 2016; Lorand et al., 2010; Luguet et al.,
820 2003), highly variable grain size (< 20 μm to 500 μm) of sulfides is widely observed in the upper
821 mantle, while most sulfides are likely smaller than about 100 μm in diameter. Hence, it is
822 plausible that almost all sulfide droplets are stranded among the crystal framework of the upper
823 peridotite mantle with low porosity, while the high-degree partial melting and/or melt-peridotite
824 reaction will lead to high porosity, large flow velocity, and even the new-forming melt channel,
825 which proposes that efficient entrainment of most sulfide droplets into ascending magma flow
826 among porous peridotite is physically possible, especially among the channelized extraction of
827 silicate melt in melt-peridotite reaction. Conceivably, the mechanical entrainment of sulfide
828 droplets during the melt-rock reaction would be more efficient than the transport of sulfide liquid
829 by dissolving in departing silicate melt. The sub-continental lithospheric mantle that undergoes
830 large-scale partial melting and melt-peridotite reaction under tectonically active craton margins
831 may be favorable conjunction of these factors and potentially conducive to the entrainment of
832 large sulfide droplets, thereby contributing to the fertilization of sub-continental lithospheric
833 mantle and the primary enrichment of metal-bearing sulfides for magmatic sulfide deposits (*e.g.*,
834 Griffin et al., 2013). This may be one of the reasons to account for the issue of why the spatial
835 and temporal distribution of magmatic Ni-Cu-(PGE) sulfide deposits are genetically related to
836 these regions (Maier and Groves, 2011).

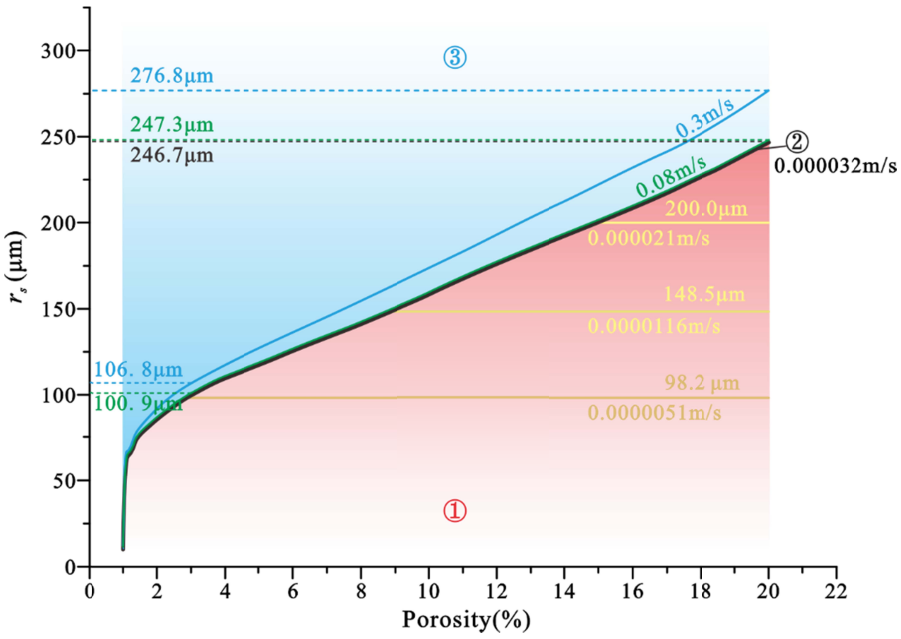

Figure 11. Plots of the radius (r_s) of initial undeformed sulfide droplets that could extrude the pore throat as a function of the porosity (Φ) of the partially molten mantle. The relationship between r_s and Φ is divided into three parts according to the relative size of sulfide droplets' radius (r_s) and the pore throat's minimum constriction (R). At $r_s < R$, the relationship is shown in region No. 1, whereas regions No. 2 and No.3 are respectively under the conditions of $r_s = R$ and $r_s > R$.

5 Conclusions

Reaction-infiltration of silicate melt and concomitant transport of sulfide droplets in the partially molten peridotite are examined experimentally and thermodynamical-quantitatively in this study, which provides important insights into the fertilization of sub-continental lithospheric mantle and the efficient recycling of sulfur and metal elements from the partially molten mantle. The reaction between peridotite and basalt leads to the preferential dissolution of olivine and the precipitation of orthopyroxene at high temperature (1250-1300 ℃) and pressure (1.5 GPa), forming an orthopyroxene-rich reaction layer (ORL) with a high growth rate (~ 0.78 ± 0.05 $\mu m/s^{0.5}$ at 1250 ℃) in the melt-rock interface. With increasing the degree of melt-peridotite reaction, more silicate melt infiltrates through the ORL into the upper partially molten peridotite, forming an olivine-melt layer above the ORL, and coarse sulfide droplets could also be entrained along with the infiltration of silicate melt. Systematic variations observed in the compositions of

minerals and reactive melt are approximately consistent with the thermodynamically-constrained mixing model. Meanwhile, the sizes of sulfide droplets have fast growth in the melt source, which is partly attributed to the multiple coarsening processes (including the mechanical coalescence) of sulfide droplets in the dynamic reactive melt flow.

Suspension and entrainment of sulfide droplets in the partially molten peridotite indicate a fast-flowing velocity of reactive melt (~ 170.9 μm/h) in our experiments, which demonstrates the occurrence of focused melt flows with high velocity in the reactive-forming melt channels, besides the melt porous flow driven by the density difference between silicate melt and minerals forming the crystal framework. It is convincible that the melt flow velocity within the melt-rock reaction is potentially high enough to drive the upward transport of fine μm-scale sulfide droplets with smaller diameters than that of the pore throat in the partially molten peridotite. In this condition, the maximum size of sulfide for upward entrainment is limited by the radius of pore throat in the crystal framework of peridotite and increases with the growth of porosity during partial melting and melt-peridotite reaction. Only in channelized melt flow with extremely high velocity, coarse-grained sulfide droplets could upward migrate through the pore throats narrower than themselves. Hence, the high-degree melt-rock reaction regions in the upper mantle, such as the sub-continental lithospheric mantle of craton margins, are likely to have wide pore throats, high porosity, and even channelized melt flow with high velocity, which can potentially drive upward entrainment and/or extrusion of μm- to mm-scale sulfide droplets in the partially molten mantle, and thereby fertilize the lithospheric mantle and lead to the endowment of Cu- and Ni-bearing sulfide for the formation of associated deposits.

Acknowledgements

We are grateful to anonymous reviewers for their useful suggestions and comments. We thank Prof. Zhang Jinsen and Dr. Wenlong Liu for their help with EPMA and EBSD analysis. Especially, I appreciate my wife Shasha Guo for the support and help in my life, so that I could do my research without any worries. This research was supported by the National Natural Science Foundation of China (No. 42102057, 42272084, and 41902088), the Natural Science Foundation of Hebei Province (No. D2021402019), the fund from SinoProbe Laboratory (No. SinoProbe Lab 202219), and the Education Department Foundation of Hebei Province of China (BJ2020023).

Data Availability Statement

All data are shown in figures, supplemental materials, and tables can also be found in the Supporting Information.

References

Aharonov, E. (1995). Channeling instability of upwelling melt in the mantle. *Journal of Geophysical Research: Solid Earth*, *100*(B10), 20433–20450. https://doi.org/10.1029/95JB01307

Alard, O., Lorand, J. P., Reisberg, L., Bodinier, J. L., Dautria, J. M., & O'Reilly, S. Y. (2011). Volatile-rich metasomatism in Montferrier xenoliths (Southern France): Implications for the abundances of chalcophile and highly siderophile elements in the subcontinental mantle. *Journal of Petrology*, *52*(10), 2009–2045. https://doi.org/10.1093/petrology/egr038

Ave Lallemant, H. G., Mercier, J.-C. C., Carter, N. L., & Ross, J. V. (1980). Rheology of the upper mantle: Inferences from peridotite xenoliths. *Tectonophysics*, *70*(1–2), 85–113. https://doi.org/10.1016/0040-1951(80)90022-0

Bagdassarov, N., Solferino, G., Golabek, G. J., & Schmidt, M. W. (2009). Centrifuge assisted percolation of Fe–S melts in partially molten peridotite: Time constraints for planetary core formation. *Earth and Planetary Science Letters*, *288*(1–2), 84–95. https://doi.org/10.1016/j.epsl.2009.09.010

Ballhaus, C., Bockrath, C., Wohlgemuth-Ueberwasser, C., Laurenz, V., & Berndt, J. (2006). Fractionation of the noble metals by physical processes. *Contributions to Mineralogy and Petrology*, *152*(6), 667–684. https://doi.org/10.1007/s00410-006-0126-z

Bauman, R. P., & Schwaneberg, R. (1994). Interpretation of Bernoulli's equation. *The Physics Teacher*, *32*(8), 478–488. https://doi.org/10.1119/1.2344087

Bockrath, C., Ballhaus, C., & Holzheid, A. (2004). Fractionation of the platinum-group elements during mantle melting. *Science*, *305*(5692), 1951–1953. https://doi.org/10.1126/science.1100160

Cascio, M. Lo, Liang, Y., Shimizu, N., & Hess, P. C. (2008). An experimental study of the grain-scale processes of peridotite melting: Implications for major and trace element distribution during equilibrium and disequilibrium melting. *Contributions to Mineralogy and Petrology*, *156*(1), 87–102. https://doi.org/10.1007/s00410-007-0275-8

916 Chadam, J., Hoff, D., Merino, E., Ortoleva, P., & Sen, A. (1986). Reactive infiltration
917 instabilities. *IMA Journal of Applied Mathematics (Institute of Mathematics and Its*
918 *Applications)*, *36*(3), 207–221. https://doi.org/10.1093/imamat/36.3.207
919 Chen, C., Yao, Z.S., Wang, C.Y. (2022). Partitioning behaviors of cobalt and manganese along
920 diverse melting paths of peridotitic and MORB-like pyroxenitic mantle. Journal of Petrology,
921 63, 1-22. https://doi.org/10.1093/petrology/egac021
922 Chung, H. Y., & Mungall, J. E. (2009). Physical constraints on the migration of immiscible
923 fluids through partially molten silicates, with special reference to magmatic sulfide ores. *Earth*
924 *and Planetary Science Letters*, *286*(1–2), 14–22. https://doi.org/10.1016/j.epsl.2009.05.041
925 Ciazela, J., Koepke, J., Dick, H. J. B., Botcharnikov, R., Muszynski, A., Lazarov, M., et al.
926 (2018). Sulfide enrichment at an oceanic crust-mantle transition zone: Kane Megamullion
927 (23°N, MAR). *Geochimica et Cosmochimica Acta*, *230*, 155–189.
928 https://doi.org/10.1016/j.gca.2018.03.027
929 Connolly, J. A. D., Schmidt, M. W., Solferino, G., & Bagdassarov, N. (2009). Permeability of
930 asthenospheric mantle and melt extraction rates at mid-ocean ridges. *Nature*, *462*(7270), 209–
931 212. https://doi.org/10.1038/nature08517
932 Daines, M. J., & Kohlstedt, D. L. (1994). The transition from porous to channelized flow due to
933 melt/rock reaction during melt migration. *Geophysical Research Letters*, *21*(2), 145–148.
934 https://doi.org/10.1029/93GL03052
935 de Bremond d'Ars, J., Arndt, N. T., & Hallot, E. (2001). Analog experimental insights into the
936 formation of magmatic sulfide deposits. *Earth and Planetary Science Letters*, *186*(3–4), 371–
937 381. https://doi.org/10.1016/S0012-821X(01)00254-0
938 Di Genova, D., Romano, C., Alletti, M., Misiti, V., & Scarlato, P. (2014). The effect of CO_2 and
939 H_2O on Etna and Fondo Riccio (Phlegrean Fields) liquid viscosity, glass transition
940 temperature and heat capacity. *Chemical Geology*, *377*, 72–86.
941 https://doi.org/10.1016/j.chemgeo.2014.04.001
942 Ding, S., & Dasgupta, R. (2017). The fate of sulfide during decompression melting of peridotite
943 – implications for sulfur inventory of the MORB-source depleted upper mantle. *Earth and*
944 *Planetary Science Letters*, *459*, 183–195. https://doi.org/10.1016/j.epsl.2016.11.020
945 Dingwell, D. B. (1996). Volcanic Dilemma--Flow or Blow? *Science*, *273*(5278), 1054–1055.
946 https://doi.org/10.1126/science.273.5278.1054

947 Farquhar, J., Wing, B. A., McKeegan, K. D., Harris, J. W., Cartigny, P., & Thiemens, M. H.
948 (2002). Mass-independent sulfur of inclusions in diamond and sulfur recycling on early Earth.
949 *Science*, *298*(5602), 2369–2372. https://doi.org/10.1126/science.1078617
950 Faul, U. H. (2001). Melt retention and segregation beneath mid-ocean ridges. *Nature*, *410*(6831),
951 920–923. https://doi.org/10.1038/35073556
952 Faul, U. H., & Scott, D. (2006). Grain growth in partially molten olivine aggregates.
953 *Contributions to Mineralogy and Petrology*, *151*(1), 101–111. https://doi.org/10.1007/s00410-
954 005-0048-1
955 Freda, C., Baker, D. R., & Scarlato, P. (2005). Sulfur diffusion in basaltic melts. *Geochimica et*
956 *Cosmochimica Acta*, *69*(21), 5061–5069. https://doi.org/10.1016/j.gca.2005.02.002
957 Ghiorso, M. S., & Sack, R. O. (1995). Chemical mass transfer in magmatic processes IV. A
958 revised and internally consistent thermodynamic model for the interpolation and extrapolation
959 of liquid-solid equilibria in magmatic systems at elevated temperatures and pressures.
960 *Contributions to Mineralogy and Petrology*, *119*(2–3), 197–212.
961 https://doi.org/10.1007/BF00307281
962 Ghiorso, M. S., Hirschmann, M. M., Reiners, P. W., & Kress, V. C. (2002). The pMELTS: A
963 revision of MELTS for improved calculation of phase relations and major element partitioning
964 related to partial melting of the mantle to 3 GPa. *Geochemistry, Geophysics, Geosystems*, *3*(5),
965 1–35. https://doi.org/10.1029/2001gc000217
966 Giordano, D., Russell, J. K., & Dingwell, D. B. (2008). Viscosity of magmatic liquids: A model.
967 *Earth and Planetary Science Letters*, *271*(1–4), 123–134.
968 https://doi.org/10.1016/j.epsl.2008.03.038
969 Griffin, W. L., Begg, G. C., & O'Reilly, S. Y. (2013). Continental-root control on the genesis of
970 magmatic ore deposits. *Nature Geoscience*, *6*(11), 905–910. https://doi.org/10.1038/ngeo1954
971 Heinrich, C. A., & Connolly, J. A. D. (2022). Physical transport of magmatic sulfides promotes
972 copper enrichment in hydrothermal ore fluids. *Geology*, *50*(10), 1101–1105.
973 https://doi.org/10.1130/G50138.1
974 Higgins, M. D. (1998). Origin of Anorthosite by Textural Coarsening: Quantitative
975 Measurements of a Natural Sequence of Textural Development. *Journal of Petrology*, *39*(7),
976 1307–1323. https://doi.org/10.1093/petrology/39.7.1307

977 Higgins, M. D. (2011). Textural coarsening in igneous rocks. *International Geology Review*,
978 *53*(3–4), 354–376. https://doi.org/10.1080/00206814.2010.496177
979 Holwell, D. A., Fiorentini, M. L., Knott, T. R., McDonald, I., Blanks, D. E., Campbell McCuaig,
980 T., & Gorczyk, W. (2022). Mobilisation of deep crustal sulfide melts as a first order control on
981 upper lithospheric metallogeny. *Nature Communications*, *13*(1).
982 https://doi.org/10.1038/s41467-022-28275-y
983 Holzheid, A. (2010). Separation of sulfide melt droplets in sulfur saturated silicate liquids.
984 *Chemical Geology*, *274*(3–4), 127–135. https://doi.org/10.1016/j.chemgeo.2010.03.005
985 Holzheid, A., & Grove, T. L. (2002). Sulfur saturation limits in silicate melts and their
986 implications for core formation scenarios for terrestrial planets. *American Mineralogist*, *87*(2–
987 3), 227–237. https://doi.org/10.2138/am-2002-2-304
988 Holzheid, A., Schmitz, M. D., & Grove, T. L. (2000). Textural equilibria of iron sulfide liquids
989 in partly molten silicate aggregates and their relevance to core formation scenarios. *Journal of*
990 *Geophysical Research: Solid Earth*, *105*(B6), 13555–13567.
991 https://doi.org/10.1029/2000JB900046
992 Honour, V. C., Holness, M. B., Partridge, J. L., & Charlier, B. (2019). Microstructural evolution
993 of silicate immiscible liquids in ferrobasalts. *Contributions to Mineralogy and Petrology*,
994 *174*(9). https://doi.org/10.1007/s00410-019-1610-6
995 Iacono-Marziano, G., Le Vaillant, M., Godel, B. M., Barnes, S. J., & Arbaret, L. (2022). The
996 critical role of magma degassing in sulphide melt mobility and metal enrichment. *Nature*
997 *Communications*, *13*(1). https://doi.org/10.1038/s41467-022-30107-y
998 Jackson, M. D., Blundy, J., & Sparks, R. S. J. (2018). Chemical differentiation, cold storage and
999 remobilization of magma in the Earth's crust. *Nature*, *564*(7736), 405–409.
1000 https://doi.org/10.1038/s41586-018-0746-2
1001 Karato, S.-I. (1984). Grain-size distribution and rheology of the upper mantle. *Tectonophysics*,
1002 *104*(1–2), 155–176. https://doi.org/10.1016/0040-1951(84)90108-2
1003 Katz, R. F., Jones, D. W. R., Rudge, J. F., & Keller, T. (2022). Physics of Melt Extraction from
1004 the Mantle: Speed and Style. *Annual Review of Earth and Planetary Sciences*, *50*, 507–540.
1005 https://doi.org/10.1146/annurev-earth-032320-083704

1006 Kelemen, P. B., Shimizu, N., & Salters, V. J. M. (1995). Extraction of mid-ocean-ridge basalt
1007 from the upwelling mantle by focused flow of melt in dunite channels. *Nature*, *375*(6534),
1008 747–753. https://doi.org/10.1038/375747a0
1009 Kress, V., Greene, L. E., Ortiz, M. D., & Mioduszewski, L. (2008). Thermochemistry of sulfide
1010 liquids IV: Density measurements and the thermodynamics of O-S-Fe-Ni-Cu liquids at low to
1011 moderate pressures. *Contributions to Mineralogy and Petrology*, *156*(6), 785–797.
1012 https://doi.org/10.1007/s00410-008-0315-z
1013 Lambart, S., Laporte, D., Provost, A., & Schiano, P. (2012). Fate of pyroxenite-derived melts in
1014 the peridotitic mantle: Thermodynamic and experimental constraints. *Journal of Petrology*,
1015 *53*(3), 451–476. https://doi.org/10.1093/petrology/egr068
1016 Lautze, N. C., Sisson, T. W., Mangan, M. T., & Grove, T. L. (2011). Segregating gas from melt:
1017 An experimental study of the Ostwald ripening of vapor bubbles in magmas. *Contributions to*
1018 *Mineralogy and Petrology*, *161*(2), 331–347. https://doi.org/10.1007/s00410-010-0535-x
1019 Lee, C. T. A., & Tang, M. (2020). How to make porphyry copper deposits. *Earth and Planetary*
1020 *Science Letters*, *529*, 115868. https://doi.org/10.1016/j.epsl.2019.115868
1021 Lee, J. S., & Fung, Y. C. (1969). Stokes flow around a circular cylindrical post confined between
1022 two parallel plates. *Journal of Fluid Mechanics*, *37*(4), 657–670.
1023 https://doi.org/10.1017/S0022112069000796
1024 Liang, Y. (1999). Diffusive dissolution in ternary systems: Analysis with applications to quartz
1025 and quartzite dissolution in molten silicates. *Geochimica et Cosmochimica Acta*, *63*(23–24),
1026 3983–3995. https://doi.org/10.1016/s0016-7037(99)00203-3
1027 Lifshitz, I. M., & Slyozov, V. V. (1961). The kinetics of precipitation from supersaturated solid
1028 solutions. *Journal of Physics and Chemistry of Solids*, *19*(1–2), 35–50.
1029 https://doi.org/10.1016/0022-3697(61)90054-3
1030 Liu, Y., Samaha, N.-T., & Baker, D. R. (2007). Sulfur concentration at sulfide saturation (SCSS)
1031 in magmatic silicate melts. *Geochimica et Cosmochimica Acta*, *71*(7), 1783–1799.
1032 https://doi.org/10.1016/j.gca.2007.01.004
1033 Lorand, J. P., & Luguet, A. (2016). Chalcophile and siderophile elements in Mantle Rocks:
1034 Trace elements controlled by trace minerals. *Reviews in Mineralogy and Geochemistry*, *81*(1),
1035 441–488. https://doi.org/10.2138/rmg.2016.81.08

1036 Lorand, J. P., Alard, O., & Luguet, A. (2010). Platinum-group element micronuggets and
1037 refertilization process in Lherz orogenic peridotite (northeastern Pyrenees, France). *Earth and*
1038 *Planetary Science Letters*, *289*(1–2), 298–310. https://doi.org/10.1016/j.epsl.2009.11.017
1039 Luguet, A., Lorand, J. P., & Seyler, M. (2003). Sulfide petrology and highly siderophile element
1040 geochemistry of abyssal peridotites: A coupled study of samples from the Kane Fracture Zone
1041 (45°W 23°20N, MARK area, Atlantic Ocean). *Geochimica et Cosmochimica Acta*, *67*(8),
1042 1553–1570. https://doi.org/10.1016/S0016-7037(02)01133-X
1043 Mallik, A., & Dasgupta, R. (2012). Reaction between MORB-eclogite derived melts and fertile
1044 peridotite and generation of ocean island basalts. *Earth and Planetary Science Letters*, *329–*
1045 *330*, 97–108. https://doi.org/10.1016/j.epsl.2012.02.007
1046 Mavrogenes, J. A., & O'Neill, H. S. C. (1999). The relative effects of pressure, temperature and
1047 oxygen fugacity on the solubility of sulfide in mafic magmas. *Geochimica et Cosmochimica*
1048 *Acta*, *63*(7–8), 1173–1180. https://doi.org/10.1016/S0016-7037(98)00289-0
1049 Mckenzie, D. (1984). The generation and compaction of partially molten rock. *Journal of*
1050 *Petrology*, *25*(3), 713–765. https://doi.org/10.1093/petrology/25.3.713
1051 McKenzie, D. (1989). Some remarks on the movement of small melt fractions in the mantle.
1052 *Earth and Planetary Science Letters*, *95*(1–2), 53–72. https://doi.org/10.1016/0012-
1053 821X(89)90167-2
1054 McKenzie, D. (2000). Constraints on melt generation and transport from U-series activity ratios.
1055 *Chemical Geology*, *162*(2), 81–94. https://doi.org/10.1016/S0009-2541(99)00126-6
1056 Médard, E., McCammon, C. A., Barr, J. A., & Grove, T. L. (2008). Oxygen fugacity,
1057 temperature reproducibility, and H_2O contents of nominally anhydrous piston-cylinder
1058 experiments using graphite capsules. *American Mineralogist*, *93*(11–12), 1838–1844.
1059 https://doi.org/10.2138/am.2008.2842
1060 Mei, S., Bai, W., Hiraga, T., & Kohlstedt, D. L. (2002). Influence of melt on the creep behavior
1061 of olivine-basalt aggregates under hydrous conditions. *Earth and Planetary Science Letters*,
1062 *201*(3–4), 491–507. https://doi.org/10.1016/S0012-821X(02)00745-8
1063 Mercier, M., Muro, A. di, Métrich, N., Giordano, D., Belhadj, O., & Mandeville, C. W. (2010).
1064 Spectroscopic analysis (FTIR, Raman) of water in mafic and intermediate glasses and glass
1065 inclusions. *Geochimica et Cosmochimica Acta*, *74*(19), 5641–5656.
1066 https://doi.org/10.1016/j.gca.2010.06.020

1067 Milke, R., Abart, R., Kunze, K., Koch-Müller, M., Schmid, D., & Ulmer, P. (2009). Matrix
1068 rheology effects on reaction rim growth I: Evidence from orthopyroxene rim growth
1069 experiments. *Journal of Metamorphic Geology*, *27*(1), 71–82. https://doi.org/10.1111/j.1525-
1070 1314.2008.00804.x
1071 Miller, K. J., Zhu, W. lu, Montési, L. G. J., & Gaetani, G. A. (2014). Experimental quantification
1072 of permeability of partially molten mantle rock. *Earth and Planetary Science Letters*, *388*,
1073 273–282. https://doi.org/10.1016/j.epsl.2013.12.003
1074 Mitchell, A. L., & Grove, T. L. (2016). Experiments on melt–rock reaction in the shallow mantle
1075 wedge. *Contributions to Mineralogy and Petrology*, *171*(12). https://doi.org/10.1007/s00410-
1076 016-1312-2
1077 Morgan, Z., & Liang, Y. (2003). An experimental and numerical study of the kinetics of
1078 harzburgite reactive dissolution with applications to dunite dike formation. *Earth and*
1079 *Planetary Science Letters*, *214*(1–2), 59–74. https://doi.org/10.1016/S0012-821X(03)00375-3
1080 Morgan, Z., & Liang, Y. (2005). An experimental study of the kinetics of lherzolite reactive
1081 dissolution with applications to melt channel formation. *Contributions to Mineralogy and*
1082 *Petrology*, *150*(4), 369–385. https://doi.org/10.1007/s00410-005-0033-8
1083 Mungall, J. E., Brenan, J. M., Godel, B., Barnes, S. J., & Gaillard, F. (2015). Transport of metals
1084 and sulphur in magmas by flotation of sulphide melt on vapour bubbles. *Nature Geoscience*,
1085 *8*(3), 216–219. https://doi.org/10.1038/ngeo2373
1086 Mungall, J. E. (2002). Empirical models relating viscosity and tracer diffusion in magmatic
1087 silicate melts. *Geochimica et Cosmochimica Acta*, *66*(1), 125–143.
1088 https://doi.org/10.1016/S0016-7037(01)00736-0
1089 Mungall, J. E., & Brenan, J. M. (2014). Partitioning of platinum-group elements and Au between
1090 sulfide liquid and basalt and the origins of mantle-crust fractionation of the chalcophile
1091 elements. *Geochimica et Cosmochimica Acta*, *125*, 265–289.
1092 https://doi.org/10.1016/j.gca.2013.10.002
1093 Niu, Y. (2004). Bulk-rock major and trace element compositions of abyssal peridotites:
1094 Implications for mantle melting, melt extraction and post-melting processes beneath Mid-
1095 Ocean ridges. *Journal of Petrology*, *45*(12), 2423–2458.
1096 https://doi.org/10.1093/petrology/egh068

1097 Patten, C., Barnes, S. J., Mathez, E. A., & Jenner, F. E. (2013). Partition coefficients of
1098 chalcophile elements between sulfide and silicate melts and the early crystallization history of
1099 sulfide liquid: LA-ICP-MS analysis of MORB sulfide droplets. *Chemical Geology*, *358*, 170–
1100 188. https://doi.org/10.1016/j.chemgeo.2013.08.040
1101 Pec, M., Holtzman, B. K., Zimmerman, M. E., & Kohlstedt, D. L. (2015). Reaction infiltration
1102 instabilities in experiments on partially molten mantle rocks. *Geology*, *43*(7), 575–578.
1103 https://doi.org/10.1130/G36611.1
1104 Pec, M., Holtzman, B. K., Zimmerman, M. E., & Kohlstedt, D. L. (2017). Reaction infiltration
1105 instabilities in mantle rocks: An experimental investigation. *Journal of Petrology*, *58*(5), 979–
1106 1003. https://doi.org/10.1093/petrology/egx043
1107 Pin, J., France, L., Lambart, S., & Reisberg, L. (2022). Thermodynamic modeling of melt
1108 addition to peridotite: Implications for the refertilization of the non-cratonic continental
1109 mantle lithosphere. *Chemical Geology*, *609*, 121050.
1110 https://doi.org/10.1016/j.chemgeo.2022.121050
1111 Rees Jones, D. W., & Rudge, J. F. (2020). Fast magma ascent, revised estimates from the
1112 deglaciation of Iceland. *Earth and Planetary Science Letters*, *542*, 116324.
1113 https://doi.org/10.1016/j.epsl.2020.116324
1114 Robertson, J. C., Barnes, S. J., & Le Vaillant, M. (2016). Dynamics of magmatic sulphide
1115 droplets during transport in silicate melts and implications for magmatic sulphide ore
1116 formation. *Journal of Petrology*, *56*(12), 2445–2472. https://doi.org/10.1093/petrology/egv078
1117 Rubin, K. H., van der Zander, I., Smith, M. C., & Bergmanis, E. C. (2005). Minimum speed limit
1118 for ocean ridge magmatism from ^{210}Pb–^{226}Ra–^{230}Th disequilibria. *Nature*, *437*(7058), 534–
1119 538. https://doi.org/10.1038/nature03993
1120 Shaw, C. S. J., Lebert, B. S., & Woodland, A. B. (2018). Thermodynamic modelling of mantle-
1121 melt interaction evidenced by veined wehrlite xenoliths from the Rockeskyllerkopf Volcanic
1122 Complex, West Eifel volcanic field, Germany. *Journal of Petrology*, *59*(1), 59–86.
1123 https://doi.org/10.1093/petrology/egy018
1124 Smith, P. M., & Asimow, P. D. (2005). Adiabat-1ph: A new public front-end to the MELTS,
1125 pMELTS, and pHMELTS models. *Geochemistry, Geophysics, Geosystems*, *6*(2), 1–8.
1126 https://doi.org/10.1029/2004GC000816

1127 Spiegelman, M., Kelemen, P. B., & Aharonov, E. (2001). Causes and consequences of flow
1128 organization during melt transport: The reaction infiltration instability in compactible media.
1129 *Journal of Geophysical Research: Solid Earth*, *106*(B2), 2061–2077.
1130 https://doi.org/10.1029/2000JB900240
1131 Sun, W. (2007). Kinetics for coarsening co-controlled by diffusion and a reversible interface
1132 reaction. *Acta Materialia*, *55*(1), 313–320. https://doi.org/10.1016/j.actamat.2006.07.045
1133 Sundberg, M., Hirth, G., & Kelemen, P. B. (2010). Trapped melt in the Josephine peridotite:
1134 Implications for permeability and melt extraction in the upper mantle. *Journal of Petrology*,
1135 *51*(1–2), 185–200. https://doi.org/10.1093/petrology/egp089
1136 Sweeney, S. M., & Martin, C. L. (2003). Pore size distributions calculated from 3-D images of
1137 DEM-simulated powder compacts. *Acta Materialia*, *51*(12), 3635–3649.
1138 https://doi.org/10.1016/S1359-6454(03)00183-6
1139 von Bargen, N., & Waff, H. S. (1986). Permeabilities, interfacial areas and curvatures of partially
1140 molten systems: Results of numerical computations of equilibrium microstructures. *Journal of*
1141 *Geophysical Research*, *91*(B9), 9261–9276. https://doi.org/10.1029/JB091iB09p09261
1142 Wagner, C. (1961). Theorie der Alterung von Niederschlägen durch Umlösen (Ostwald-
1143 Reifung). *Zeitschrift Für Elektrochemie, Berichte Der Bunsengesellschaft Für Physikalische*
1144 *Chemie*, *65*(7–8), 581–591. https://doi.org/10.1002/bbpc.19610650704
1145 Wang, C., Liang, Y., Xu, W., & Dygert, N. (2013). Effect of melt composition on basalt and
1146 peridotite interaction: Laboratory dissolution experiments with applications to mineral
1147 compositional variations in mantle xenoliths from the North China Craton. *Contributions to*
1148 *Mineralogy and Petrology*, *166*(5), 1469–1488. https://doi.org/10.1007/s00410-013-0938-6
1149 Wang, C., Liang, Y., Dygert, N., & Xu, W. (2016). Formation of orthopyroxenite by reaction
1150 between peridotite and hydrous basaltic melt: an experimental study. *Contributions to*
1151 *Mineralogy and Petrology*, *171*(8–9). https://doi.org/10.1007/s00410-016-1287-z
1152 Wang, C., Lo Cascio, M., Liang, Y., & Xu, W. (2020). An experimental study of peridotite
1153 dissolution in eclogite-derived melts: Implications for styles of melt-rock interaction in
1154 lithospheric mantle beneath the North China Craton. *Geochimica et Cosmochimica Acta*, *278*,
1155 157–176. https://doi.org/10.1016/j.gca.2019.09.022

Wang, J., Xiong, X., Zhang, L., & Takahashi, E. (2020). Element loss to platinum capsules in high-temperature-pressure experiments. *American Mineralogist*, *105*(10), 1593–1597. https://doi.org/10.2138/am-2020-7580

Wang, K.-L., O'Reilly, S. Y., Griffin, W. L., Pearson, N. J., & Zhang, M. (2009). Sulfides in mantle peridotites from Penghu Islands, Taiwan: Melt percolation, PGE fractionation, and the lithospheric evolution of the South China block. *Geochimica et Cosmochimica Acta*, *73*(15), 4531–4557. https://doi.org/10.1016/j.gca.2009.04.030

Wang, Z. J., & Jin, Z. (2020). Reaction Infiltration Instabilities in Partially Molten Peridotite and Implications for Driving the Transport of Sulfide Liquid. *Journal of Earth Science*, *31*(3), 447–455. https://doi.org/10.1007/s12583-020-1301-2

Wang, Z. J., Jin, Z., Mungall, J. E., & Xiao, X. (2020). Transport of coexisting Ni-Cu sulfide liquid and silicate melt in partially molten peridotite. *Earth and Planetary Science Letters*, *536*, 116162. https://doi.org/10.1016/j.epsl.2020.116162

Yao, Z. S., & Mungall, J. E. (2021). Kinetic controls on the sulfide mineralization of komatiite-associated Ni-Cu-(PGE) deposits. *Geochimica et Cosmochimica Acta*, *305*, 185–211. https://doi.org/10.1016/j.gca.2021.05.009

Yao, Z. S., Qin, K. Z., & Xue, S. C. (2017). Kinetic processes for plastic deformation of olivine in the Poyi ultramafic intrusion, NW China: Insights from the textural analysis of a ~ 1700 m fully cored succession. *Lithos*, *284–285*, 462–476. https://doi.org/10.1016/j.lithos.2017.05.002

Yao, Z. S., & Mungall, J. E. (2020). Flotation mechanism of sulphide melt on vapour bubbles in partially molten magmatic systems. *Earth and Planetary Science Letters*, *542*, 116298. https://doi.org/10.1016/j.epsl.2020.116298

Yao, Z. S., Qin, K. Z., & Mungall, J. E. (2018). Tectonic controls on Ni and Cu contents of primary mantle-derived magmas for the formation of magmatic sulfide deposits. *American Mineralogist*, *103*(10), 1545–1567. https://doi.org/10.2138/am-2018-6392

Yao, Z. S., Mungall, J. E., & Qin, K. Z. (2019). A preliminary model for the migration of sulfide droplets in a magmatic conduit and the significance of volatiles. *Journal of Petrology*, *60*(12), 2281–2316. https://doi.org/10.1093/petrology/egaa005

Yao, Z. S., Mungall, J. E., & Jenkins, M. C. (2021). The Rustenburg Layered Suite formed as a stack of mush with transient magma chambers. *Nature Communications*, *12*(1), 1–14. https://doi.org/10.1038/s41467-020-20778-w

1187 Yoshino, T., & Watson, E. B. (2005). Growth kinetics of FeS melt in partially molten peridotite:
1188 An analog for core-forming processes. *Earth and Planetary Science Letters*, *235*(1–2), 453–
1189 468. https://doi.org/10.1016/j.epsl.2005.04.021
1190 Yoshino, T., Walter, M. J., & Katsura, T. (2003). Core formation in planetesimals triggered by
1191 permeable flow. *Nature*, *422*(6928), 154–157. https://doi.org/10.1038/nature01459
1192 Yoshino, T., Walter, M. J., & Katsura, T. (2004). Connectivity of molten Fe alloy in peridotite
1193 based on in situ electrical conductivity measurements: Implications for core formation in
1194 terrestrial planets. *Earth and Planetary Science Letters*, *222*(2), 625–643.
1195 https://doi.org/10.1016/j.epsl.2004.03.010
1196 Yoshino, T., Laumonier, M., McIsaac, E., & Katsura, T. (2010). Electrical conductivity of
1197 basaltic and carbonatite melt-bearing peridotites at high pressures: Implications for melt
1198 distribution and melt fraction in the upper mantle. *Earth and Planetary Science Letters*,
1199 *295*(3–4), 593–602. https://doi.org/10.1016/j.epsl.2010.04.050
1200 Zhang, Y. (2015). Toward a quantitative model for the formation of gravitational magmatic
1201 sulfide deposits. *Chemical Geology*, *391*, 56–73.
1202 https://doi.org/10.1016/j.chemgeo.2014.10.025
1203 Zhang, Y., Walker, D., & Lesher, C. E. (1989). Diffusive crystal dissolution. *Contributions to*
1204 *Mineralogy and Petrology*, *102*(4), 492–513. https://doi.org/10.1007/BF00371090
1205 Zhang, Y., Ni, H., & Chen, Y. (2010). Diffusion data in silicate melts. *Reviews in Mineralogy*
1206 *and Geochemistry*, *72*(1), 311–408. https://doi.org/10.2138/rmg.2010.72.8
1207 Zhao, Y., Liu, S. A., Xue, C., & Li, M. L. (2022). Copper isotope evidence for a Cu-rich mantle
1208 source of the world-class Jinchuan magmatic Ni-Cu deposit. *American Mineralogist*, *107*(4),
1209 673–683. https://doi.org/10.2138/am-2021-7911
1210 Zhu, W., Gaetani, G. A., Fusseis, F., Montési, L. G. J., & de Carlo, F. (2011). Microtomography
1211 of partially molten rocks: Three-dimensional melt distribution in mantle peridotite. *Science*,
1212 *332*(6025), 88–91. https://doi.org/10.1126/science.1202221